

RESEARCH ARTICLE

Nonlinear control of two-stage single-phase standalone photovoltaic system

Adil Latif¹, Laiq Khan², Shahrukh Agha², Sidra Mumtaz¹, Jamshed Iqbal^{3*}

1 Department of Electrical and Computer Engineering, COMSATS University Islamabad, Abbottabad Campus, Abbottabad, KPK, Pakistan, **2** Department of Electrical and Computer Engineering, COMSATS University Islamabad, Islamabad, Pakistan, **3** School of Computer Science, Faculty of Science and Engineering, University of Hull, Hull, United Kingdom

* j.iqbal@hull.ac.uk

Abstract

This paper presents a single-phase Photovoltaic (PV) inverter with its superior and robust control in a standalone mode. Initially, modeling and layout of the Buck-Boost DC-DC converter by adopting a non-linear Robust Integral Back-stepping controller (RIBSC) is provided. The controller makes use of a reference voltage generated through the regression plane so that the operating point corresponding to the maximum power point (MPP) could be achieved through the converter under changing climatic conditions. The other main purpose of the Buck-Boost converter is to act like a transformer and produce an increased voltage at the inverter input whenever desired. By not using a transformer makes the circuit size more compact and cost-effective. The proposed RIBSC is applied to an H-bridge inverter with an LC filter to produce the sinusoidal wave in the presence of variations in the output to minimize the difference between the output voltage and the reference voltage. Lyapunov stability criterion has been used to verify the stability and finite-time convergence of the overall system. The overall system is simulated in MATLAB/Simulink to test the system performance with different loads, varying climatic conditions and inverter reference voltages. The proposed methodology is compared with a back-stepping controller and Proportional Integral Derivative (PID) controller under rapidly varying climatic conditions. Results demonstrated that the proposed technique yielded a tracking time of 0.01s, a total harmonic distortion of 9.71% and a root means square error of 0.3998 in the case of resistive load thus showing superior control performance compared to the state-of-the-art control techniques.

1. Introduction

An independent system based on renewable power resources is one of the high-quality alternatives to meet the power demand in far-off and remote areas where the application grids are difficult to access or expensive [1]. Such systems are modeled to function irrespective of the application grid, as indicated by the name. A standalone device consists of various components that transform renewable energy sources including wind and Photovoltaic (PV) energy in a controlled and reliable way into electrical charges and electrical energy.



OPEN ACCESS

Citation: Latif A, Khan L, Agha S, Mumtaz S, Iqbal J (2024) Nonlinear control of two-stage single-phase standalone photovoltaic system. PLoS ONE 19(2): e0297612. <https://doi.org/10.1371/journal.pone.0297612>

Editor: Yogendra Arya, J.C. Bose University of Science and Technology, YMCA, INDIA, INDIA

Received: July 31, 2023

Accepted: January 9, 2024

Published: February 8, 2024

Copyright: © 2024 Latif et al. This is an open access article distributed under the terms of the [Creative Commons Attribution License](https://creativecommons.org/licenses/by/4.0/), which permits unrestricted use, distribution, and reproduction in any medium, provided the original author and source are credited.

Data Availability Statement: All relevant data are within the manuscript.

Funding: The author(s) received no specific funding for this work.

Competing interests: The authors have declared that no competing interests exist.

There are two types of existing PV systems: stand-alone [2], and grid-connected [3]. To connect the DC power supply to the grid at the PV level, the use of a converter as an interface is very important [4, 5]. This system is called a PV network connected to the grid. On the other hand, stand-alone PV systems include converting PV power into AC loads to be used at the user's location. Power converters are necessary if solar-based PV modules and AC loads are to be interconnected. Such a power converter serves two main functions: First, it ensures that maximum power is generated continuously by the PV array irrespective of atmosphere, and load conditions. The second functionality is to alter the uniform voltage generated by the PV array into an AC voltage for AC load use. For example, a grid with stable repeatability, amplitude, and sinusoidal form should have identical performance and parameters for the AC output voltage. To attain these functions, several topologies are illustrated in [6, 7].

In this article, a two-phase-topology converter is being used. This requires an H-bridge inverter and buck-boost converter. The main purpose of the primary converter (buck-boost converter) is to allow the PV array to use the Maximum Power Point Tracking (MPPT) scheme to produce the maximum power [8]. Many algorithms can be used to adjust Maximum Power Point (MPP) correctly. Martin and Vazquez [9] used the back-stepping algorithm to achieve MPPT. Numerous researchers have discussed two extensive categories of MPPT technology: indirect MPP technology (such as open-circuit fractional voltage technology [10]), direct MPP technology (such as incremental conductivity [11, 12]) or Perturb and Observe (P & O) technologies. Motahhir et al. in [11] used the proposed incremental conductance to achieve a response time of 7ms to follow the appropriate power value with 97.53% efficiency. In [12], reinforcement times of 2.42ms and 2.17ms were achieved corresponding to the MPPT back-stepping control and integral back-stepping control respectively. In [13], efficiencies of 96%, 96.5%, 98.2%, and 99.1% were achieved using P & O technology, PI controller, Sliding Mode Control (SMC), neuro-fuzzy, group optimization, and back-stepping respectively. Our key goal is to obtain a shorter response time in the MPPT phase. P & O technology has the deterministic advantage, that is, the P-V curve rises on the left side of the MPP, and essentially drops on the right side of the MPP. The main drawback of this technique is that it always fluctuates around the MPP area. This problem can be reduced by making small movements around the MPP. The DC-DC converter has another defect of no output voltage regulation. Therefore, this fact must be brought into consideration as reported by Kaouane et al. in [14]. In [15], Chen et al. used various optimization techniques including Particle Swarm Optimization (PSO) to obtain the maximum power by designing an MPPT controller to enhance the efficiency of a PV inverter.

An inverter is part of the second stage of the proposed solution. To ensure the effective usage of Distributed Generation (DG) units, modeled inverters play the function of converting and adapting energy between a source and a load [16]. In these inverters, the conversion rule is to use a pulse width modulation (PWM) program to provide the load with a stable 220V (RMS) AC sinusoidal output voltage. Many inverters use electronic power switches on the output platform, for example, Insulated-Gate Bipolar Transistor (IGBTs) or Metal Oxide Semiconductor Field-effect Transistor (MOSFETs). The PWM program makes these inverters suitable for various electrical equipment [16]. Therefore, these inverters must have a minimum total harmonic distortion (THD), high efficiency, and rapid transient response. Many considerations have been made for the regulation of PWM inverters to ensure low THD, fast dynamic response, and constant frequency sinusoidal output voltage under various loads [17]. Proportional Integral Derivative (PID) control [18], sliding mode control [19], linear control [20], Lyapunov control [21], linear resonance control [22] and passive basic control [23] are the most well-recognized regulatory techniques. Zadeh et al. [24] proposed and evaluated three kinds of controllers: back-stepping, sliding mode, and fuzzy logic with the back-stepping

controller demonstrating superior performance. Kolbasi and Seker [25] proposed a nonlinear inverter controller based on robust back-stepping. However, having more than two gains makes it harder for the controller to be efficient.

The control method based on the Lyapunov function proposed for a single-phase inverter in [26] achieved global balance with no steady-state error in the output voltage. Robust back-stepping control techniques for nonlinear systems have been developed in literature [27]. The designed controller provided a smoother controller movement for dynamic systems by providing an adjustment function to achieve the reference value. For an independent single-phase voltage source inverter, a control system based on droop-Lyapunov was proposed in [28]. The control system is determined by the dynamic model inverter that has evolved in the rotating body d-q. The dynamic version and the direct Lyapunov technology were used respectively to evaluate the reliability of the controller's overall output under steady-state and dynamic operation. Therefore, a capacity curve (CC) was given to assess the most extreme positive and negative values of the inverter current component d-q.

Xue et al. [29] included a sketch of single-phase inverters generated for little-used generators. Yao et al. [30] suggested a single-phase, seamless transition of smart grid inverters between independent and grid-connected modes. Even though both independent power sources and power grid-related power sources can be attained through different circuit structures or current control plans [29, 30], the stability of the entire system cannot be demonstrated more comprehensively, and the new structure of the circuit system cannot be used correctly in commercial products. It is a difficult task for scientists and researchers to get the maximum energy possible from the existing PV system [31]. Artificial neural networks, which employ intricate sets of qualitative heuristically developed rules and extensive training data sets, tend to increase the flexibility of the controller design. To lessen or prevent the overshoot in the load current and power, sliding-mode controllers have been proposed [32]. Additionally, these controllers play a crucial role in producing a reliable response, particularly when SMCs and ANN algorithms are combined [32].

In [33], Armghan et al. presented the modeling and design of a single-phase PV inverter with MPPT algorithm applied to the boost converter using back-stepping control in the stand-alone mode. The authors also made use of a DC-to-AC converter for AC loads. The response time to attain the exact value of the power of the PV array was around 1ms and the efficiency of the MPPT system was 99.93%. The response time of the inverter has a good form of the output voltage for electrical loads was 30ms at the beginning. Moreover, with an input voltage of the inverter greater than 311V, the response time of this controller was less than 15ms that ensuring the high robustness of the designed controller. Total Harmonic Distortion (THD) reported was about 0.78%. However, the response obtained was still oscillatory.

In [34], Arsalan et al. proposed a back-stepping-based non-linear controller for MPPT in a PV system. Authors showed the achievement of MPP with little oscillations under varying irradiance and temperature conditions. The MPP is achieved in 0.02 seconds under varying irradiance and 0.04 seconds under varying temperatures conditions. Also, the proposed methodology was shown to be superior, in terms of convergence speed and ripples compared to P & O and Fuzzy logic controller techniques which suffered from ripples and oscillations respectively.

In [35], Diouri et al. used integral action in the nonlinear back-stepping controller for MPPT of a PV system. A regression plane was used to generate the tracking peak power voltage. Under varying irradiance and temperature conditions, the tracking time was reported to be 2ms with the converter efficiency of 95%. However, an overshoot of 13.8V (4.7% of steady-state value) was observed in the response under varying irradiance and a small overshoot of 7.44V (2.6% of steady-state value) was observed under varying temperature conditions. The

proposed technique was also compared with P & O and PID methods and is shown to be robust in comparison. Also, the proposed technique was compared with back-stepping and Fuzzy logic controller methods. Back-stepping method has a small steady error under varying irradiance and temperature conditions whereas the Fuzzy logic controller showed large oscillatory behavior around MPP.

In [36], Ali et al. proposed a nonlinear robust integral back-stepping-based MPPT control for a stand-alone PV system. A comparison was made with back-stepping, integral back-stepping, PID and P & O methods under three different operating conditions, including varying irradiance, temperature, and fault injections. A significant steady-state error and overshoot were reported to exist in the back-stepping (B) and integral back-stepping (IB) techniques, respectively. In comparison the proposed methodology of [36] achieves a tracking time of 0.02 seconds with 98% efficiency of the PV array. The proposed technique is also compared with PID and P & O methods and is shown to be robust with minimum chattering in comparison.

In [37] Khan et al. suggested a radial basis function (RBF) neural network-based back-stepping terminal sliding mode MPPT control technique for a stand-alone PV systems. The proposed methodology was reported to have a reduced chattering effect, improved transient response, and faster convergence, with a PV array efficiency of 98.74% when compared to the benchmarks of P & O, PID, and back-stepping controllers. From the above, it can be inferred that though the proposed methodologies have addressed the aforementioned issues under different conditions, there are still some robustness and oscillatory behavior issues, which are undesirable. For instance, the back-stepping technique is highly efficient but not robust in varying conditions.

In [38], an experimental estimation of a hybrid adaptive neuro-fuzzy inference system–particle swarm optimization (ANFIS–PSO) based MPPT for PV grid integration under fluctuating sun irradiance was presented. The method aims to achieve fast and maximal PV power with zero oscillation tracking. A space vector modulation hysteresis current controller was utilized to implement an inverter control strategy to obtain high-quality inverter current by accurately tracking the reference sine-shaped current. In [39], an extensive practical investigation of fuzzy particle swarm optimization (FPSO) based MPPT for grid-integrated PV system under variable operating conditions with anti-islanding protection was presented. Different conditions, such as varying sun irradiance, partial shadow, and loading conditions have been considered for the verification of the proposed methodology. Experimental implementation and verification of the proposed system, along with high tracking efficiency, were reported. In [40], an adaptive Takagi Sueno (TS)-fuzzy model-based radial basis function (RBF) neural network learning for grid-integrated PV applications was presented. Rapid and accurate PV power tracking is reported to have been achieved under varying solar irradiance. Keeping this in view, the significant contributions in this work are as follows:

1. A robust controller is proposed that has a fast convergence time with negligible oscillations.
2. A PV array system, comprising a DC-DC buck-boost converter and an inverter, is suggested supplying maximum power achieved to AC loads under varying irradiance and temperature conditions. Additionally, the inverter has a minimum total harmonic distortion.
3. The proposed controller is compared with state-of-the-art benchmarks, namely PID and back-stepping controllers, and is demonstrated to exhibit faster convergence time, reduced steady-state error, fewer oscillations and ripples, faster rise times, and low settling times. Various performance metrics, such as Integral Time Square Error (ITSE), Integral Time Absolute Error (ITAE), Integral Square Error (ISE), and Integral Absolute Error (IAE), have been employed to showcase the superiority of the proposed controller.

4. The proposed technique is evaluated in two different scenarios: a) Steady-state performance of the inverter output voltage with different loads b) Transient performance of the inverter output voltage when the reference amplitude changes in steps. The execution of the proposed technique is analyzed and compared with the back-stepping and PID controllers.
5. The proposed scheme is highly efficient because it can rapidly adapt to sudden changes in climatic conditions, including temperature fluctuations, variations in sunlight, or both. Regarding voltage stability, the system can consistently maintain a voltage of 220V and a stable frequency of 50Hz under changing loads.

The rest of the paper is organized into five main sections i.e. System overview and model description is presented in section 2. In addition, the non-inverting buck-boost converter and H-bridge inverter along with the average state-space layout is presented. Section 3 introduces the PV control system architecture designed to achieve full power and transform the DC voltage to the AC voltage. In section 4, the design and simulation of the proposed technique is explained, and the result of the proposed technique comparison are discussed and analyzed under different load conditions and step changes in reference amplitude. Section 5 provides the paper's conclusion, along with suggestions for future work.

2. System overview and model description

A typical model of a PV system takes into consideration economic operation and is usually comprised of a DC-AC inverter, an MPPT controller strategy, a DC-DC converter, and PV modules. The PV array and the AC loads are connected by two power electronic converters in the system. To achieve maximum power delivery to the loads and ensure proper DC to AC power conversion, both converters are controlled by a Robust Integral Back-stepping Controller (RIBSC). The first converter, using a simple MPPT algorithm to tracks the maximum electrical energy produced by the PV array under various temperatures and irradiance levels. To compel the PV array to supply this voltage, it generates the reference voltage for the controller. The second converter, equipped with an LC filter, is responsible for converting continuous voltage to alternating voltage while reducing harmonic distortion and maintaining an acceptable amplitude and frequency stability across various resistive load values. The block diagram of the simulation is depicted in Fig 1. The internal blocks of RIBSC for converter and inverter are depicted in Figs 2 and 3, respectively.

2.1 Mathematical modeling of PV system

The PV cell is configured so that it takes solar irradiance as input and generates electrical energy as output [41]. Typically, electrical equivalent models of PV cells are presented as either single-diode models [42] or two-diode models [43]. The two-diode model, being more complex, requires additional parameters to design a precise model. This research opts for a single-diode version for its simplicity. The PV cell resembles a diode with a p-n junction, which converts photons into electricity. As displayed in Fig 2, a diode model is composed of a diode D , current source I_L , shunt resistance R_C , and series resistance R_S . To determine the corresponding circuit parameters, PV voltage, current, and power curves must be observed under standard measuring conditions. Given that the value of R_C is relatively high and the value of R_S is low, these two parameters can be neglected to simplify the analysis [44]. The following equations, with the application of Kirchhoff's Current Law (KCL), describes the equivalent circuit shown in Fig 4.

$$I_{PV} = I_L - I_D - I_p \quad (1)$$

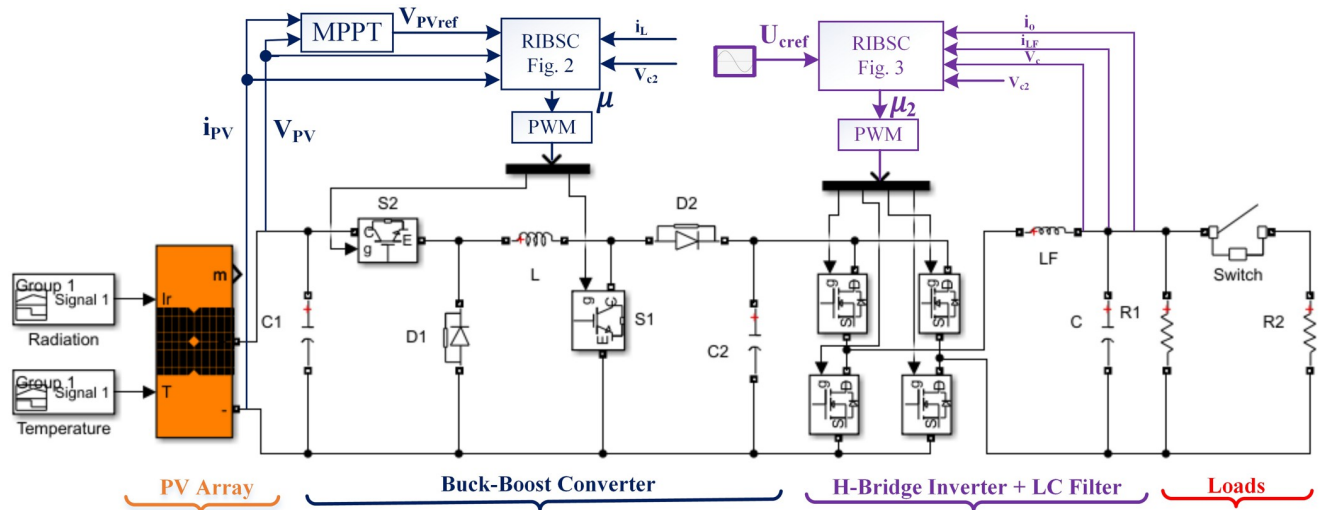


Fig 1. A standalone PV system model.

<https://doi.org/10.1371/journal.pone.0297612.g001>

where the photo-current generated by the PV cell is denoted as I_L , and it depends on the temperature (T), solar radiation, and diode current I_D . Similarly, I_p represents the shunt current, and I_{pv} is the output current in amperes of the PV cell. When a number of PV cells are connected in series and parallel, they form a PV module or panel. Eq (2) illustrates the PV module's output current I_{pv} to the output voltage V_{pv} when N_s and N_p cells are connected in series

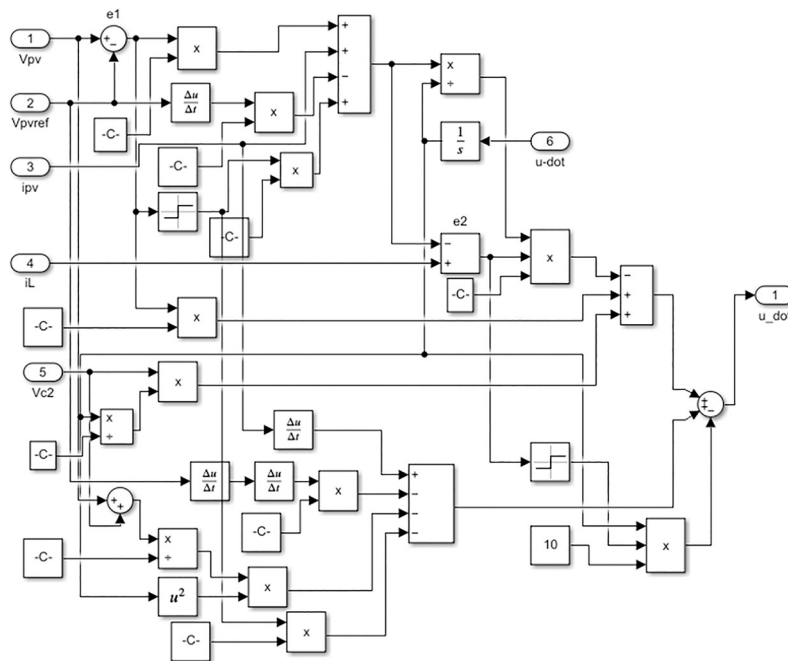


Fig 2. Internal blocks of RIBSC for converter.

<https://doi.org/10.1371/journal.pone.0297612.g002>

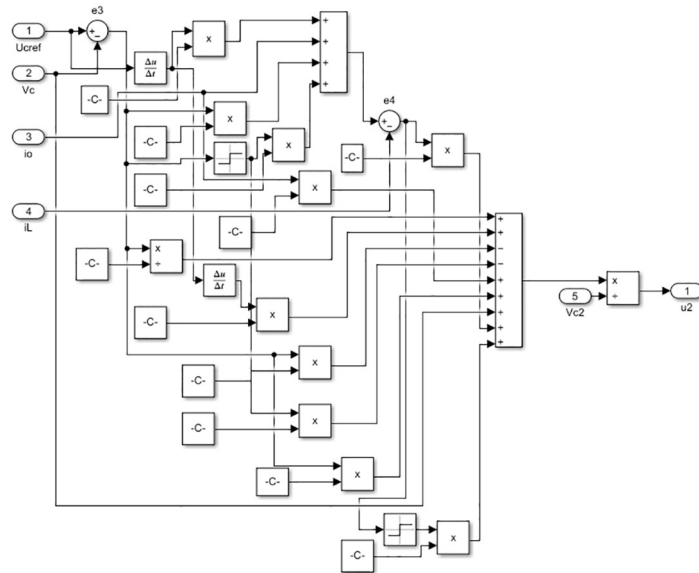


Fig 3. Internal blocks of RIBSC for inverter.

<https://doi.org/10.1371/journal.pone.0297612.g003>

and parallel, respectively [41].

$$I_{pv} = N_p I_L - N_p I_D \left[\exp \frac{qV_{pv}}{N_s A k T} - 1 \right] \tag{2}$$

where V_{pv} is the output voltage of the PV module in volts, N_p and N_s represents the PV cells connected in parallel and series, respectively. The ideality factor of a diode is denoted as A , T is the temperature in Kelvin, k is the Boltzmann constant in J/K and the electron charge is q in Coulombs. The reverse saturation current of the PV module, I_D , is given by:

$$I_D = I_{Dr} \left(\frac{T}{T_r} \right)^3 \exp \left(\frac{qE_g}{kA} \left[\frac{1}{T_r} - \frac{1}{T} \right] \right) \tag{3}$$

where $E_g = 1.1$ eV is the semiconductor band gap, and the reference temperature of the cells is

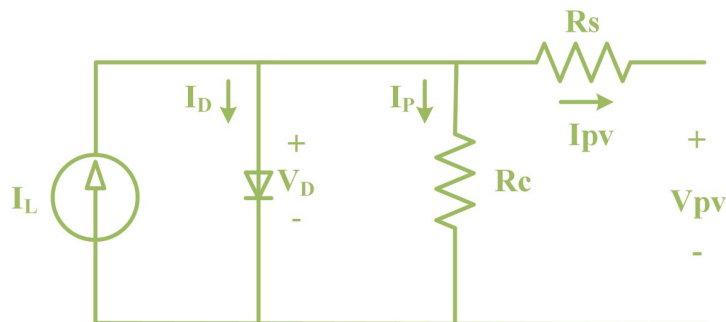


Fig 4. PV array equivalent model.

<https://doi.org/10.1371/journal.pone.0297612.g004>

T_r . Therefore, at T_r , the reverse saturation current I_{Dr} is specified by the following equation.

$$I_{Dr} = \frac{I_{scr}}{\exp\left(\frac{qV_{oc}}{N_s AkT}\right) - 1} \tag{4}$$

Among them, V_{OC} is the open-circuit voltage, and I_{scr} is the short-circuit current of the PV module at the reference temperature T_r . The dependence of I_L on temperature and solar irradiance is described by the following equations.

$$I_L = [I_{scr} + K_i(T - T_r)] \frac{E}{100} \tag{5}$$

where $K_i[A/K]$ is the temperature coefficient of I_{SCR} .

A mathematical description of the output power of a PV module, derived from Eq (2), is coined below.

$$P_{pv} = I_{pv} V_{pv} \tag{6}$$

$$P_{pv} = N_p I_{ph} V_{pv} - N_p I_D V_{pv} \left[\exp\left(\frac{qV_{pv}}{N_s AkT}\right) - 1 \right] \tag{7}$$

The PV array considered in this article is composed of four strings that can be connected in parallel. Each string includes series-connected four modules. Thus, the overall amount of PV modules utilized is sixteen. Each module has an intensity of 1555W. Therefore, the maximum power provided by the system is $16 \times 1555 = 24,880W$. Figs 5 and 6 shows the PV array's (I-V) and (P-V) characteristics for various temperature (T) and irradiance values, respectively.

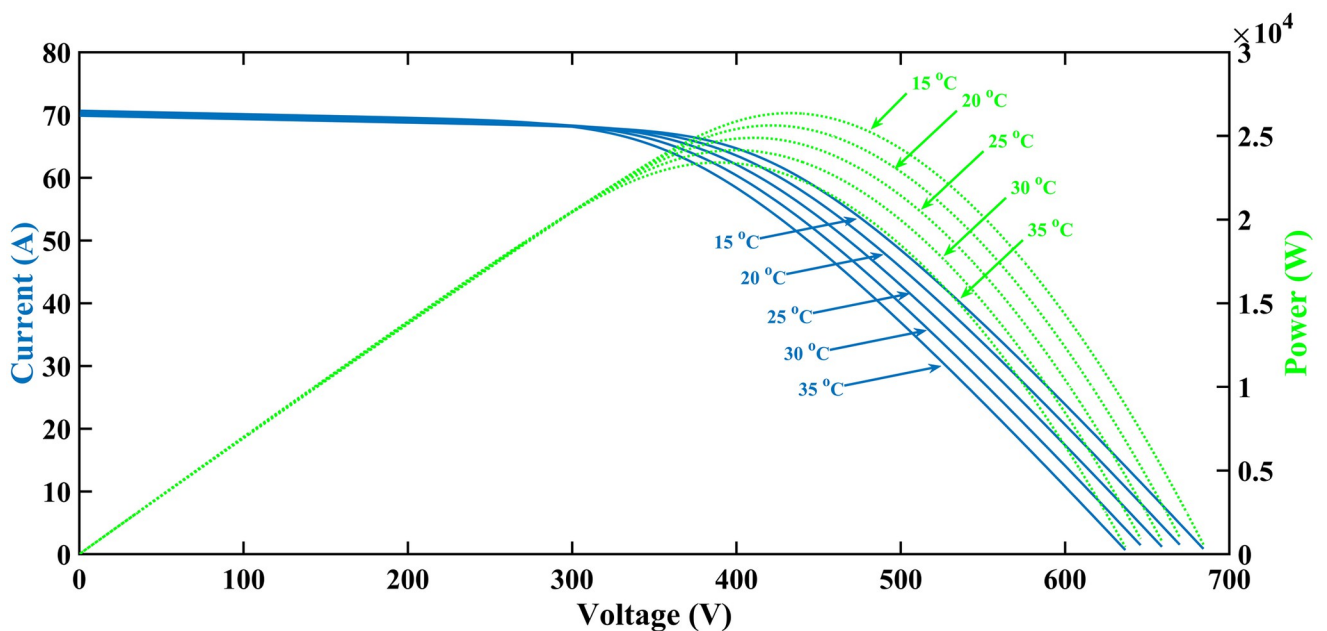


Fig 5. I-V and P-V characteristics curves at rising temperature.

<https://doi.org/10.1371/journal.pone.0297612.g005>

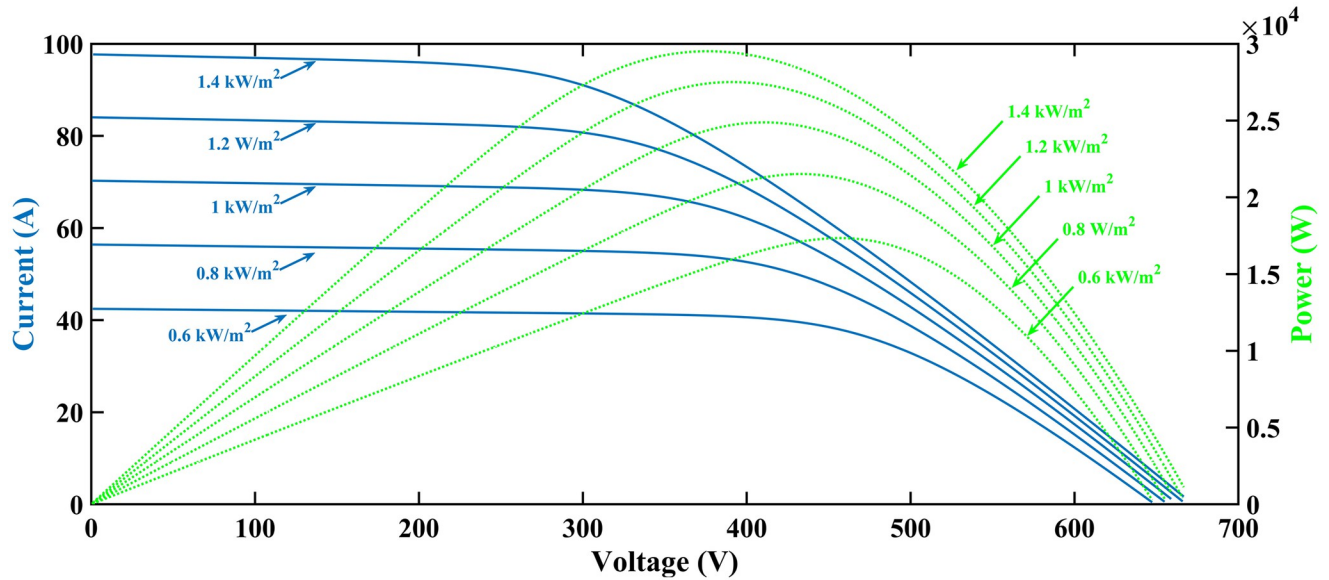


Fig 6. I-V and P-V characteristics curves at rising irradiance.

<https://doi.org/10.1371/journal.pone.0297612.g006>

2.2 Mathematical modeling of non-inverting DC to DC buck-boost converter

The output voltage V_{PV} of the PV array can be raised or lowered using a designed converter to match the reference voltage V_{PVref} . The non-inverting buck-boost converter is responsible for tracking the maximum electrical energy produced by the PV array at various temperatures and irradiance levels to meet the reference voltage for the back-stepping controller. Fig 7 demonstrates the in-phase DC-DC buck-boost converter circuit topology. The output voltage can be regulated by changing the converter’s duty cycle to maximize output power through designed controllers. The converter operates in continuous conduction mode (CCM) while assuming ideal semiconductor switches and diodes [45].

This converter is commonly used in applications that require low cost and compact component size. The converter is continuously controlled through its changing period T , where: $T = t_{on} + t_{off}$ and $\mu = t_{on}/T$ is defined as the converter duty ratio. Input voltage ripples of the converter are limited by the input capacitor C_1 , and output voltage ripples are restricted by C_2 . The switching operation involves two periods. First, diodes D_1 and D_2 are in reverse bias, while switches S_1 and S_2 are both in conduction mode. In the second period, switches S_1 and S_2 are turned OFF, and D_1 and D_2 are forward biased. The state-space equation for mode 1, when switches are in conduction mode and the diodes are reverse biased, can be represented in matrix form as follows:

$$\begin{bmatrix} \frac{d}{dt} V_{PV} \\ \frac{d}{dt} i_L \\ \frac{d}{dt} V_{c2} \end{bmatrix} = \begin{bmatrix} 0 & -\frac{1}{C_1} & 0 \\ \frac{1}{L} & 0 & 0 \\ 0 & 0 & -\frac{1}{R_L C_2} \end{bmatrix} \begin{bmatrix} V_{PV} \\ i_L \\ V_{c2} \end{bmatrix} + \begin{bmatrix} \frac{i_{PV}}{C_1} \\ 0 \\ 0 \end{bmatrix} \quad (8)$$

The state-space equation for mode 2, when diodes are forward-biased and switches are OFF.

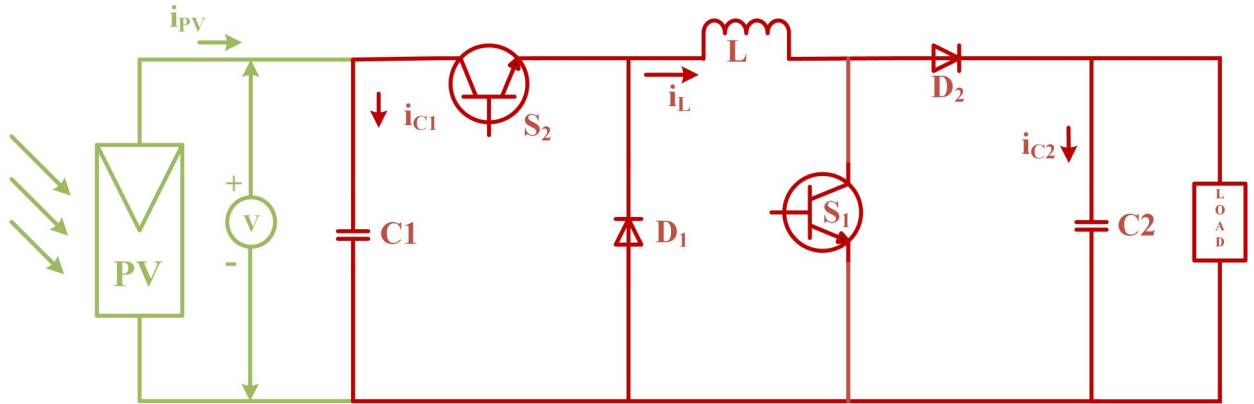


Fig 7. Non-inverting DC-DC buck-boost circuit topology.

<https://doi.org/10.1371/journal.pone.0297612.g007>

The equation in matrix form is given as:

$$\begin{bmatrix} \frac{d}{dt} V_{PV} \\ \frac{d}{dt} i_L \\ \frac{d}{dt} V_{c2} \end{bmatrix} = \begin{bmatrix} 0 & 0 & 0 \\ 0 & 0 & -\frac{1}{L} \\ 0 & \frac{1}{C_2} & -\frac{1}{R_L C_2} \end{bmatrix} \begin{bmatrix} V_{PV} \\ i_L \\ V_{c2} \end{bmatrix} + \begin{bmatrix} \frac{i_{PV}}{C_1} \\ 0 \\ 0 \end{bmatrix} \tag{9}$$

Now, the average model of the non-inverting DC-DC buck-boost converter in the form of a vector matrix is as follows, based on volt-second balance and capacitor charge level:

$$\begin{bmatrix} \frac{d}{dt} V_{PV} \\ \frac{d}{dt} i_L \\ \frac{d}{dt} V_{c2} \end{bmatrix} = \begin{bmatrix} 0 & -\frac{\mu}{C_1} & 0 \\ \frac{\mu}{L} & 0 & \frac{\mu}{L} - \frac{1}{L} \\ 0 & \frac{1}{C_2} & -\frac{1}{R_L C_2} \end{bmatrix} \begin{bmatrix} V_{PV} \\ i_L \\ V_{c2} \end{bmatrix} + \begin{bmatrix} \frac{i_{PV}}{C_1} \\ 0 \\ 0 \end{bmatrix} \tag{10}$$

Considering x_1 , x_2 , and x_3 as the average values of V_{PV} , i_L , and V_{C2} , respectively. Under the assumption, the state representation is as follows:

$$\begin{bmatrix} \dot{x}_1 \\ \dot{x}_2 \\ \dot{x}_3 \end{bmatrix} = \begin{bmatrix} 0 & -\frac{\mu}{C_1} & 0 \\ \frac{\mu}{L} & 0 & \frac{\mu}{L} - \frac{1}{L} \\ 0 & \frac{1}{C_2} - \frac{\mu}{C_2} & -\frac{1}{R_L C_2} \end{bmatrix} \begin{bmatrix} x_1 \\ x_2 \\ x_3 \end{bmatrix} + \begin{bmatrix} \frac{i_{PV}}{C_1} \\ 0 \\ 0 \end{bmatrix} \tag{11}$$

Interpretation from matrix shape to equation form is as follows:

$$\dot{x}_1 = \frac{i_{PV}}{C_1} - \frac{\mu x_2}{C_1} \tag{12}$$

$$\dot{x}_2 = -\frac{x_3}{L} + \mu \frac{x_1 + x_3}{L} \tag{13}$$

$$\dot{x}_3 = -\frac{x_2}{C_2} - \frac{x_3}{R_L C_2} - \frac{\mu x_2}{C_2} \tag{14}$$

A buck-boost converter model that does not invert is required. The Converter’s voltage

transformation ratio is:

$$\frac{V_{c2}}{V_{PV}} = \frac{\mu}{1 - \mu} \quad (15)$$

The reflected input impedance on an ideal transfer of power is provided by [33],

$$R_{out} = R_{in} \quad (16)$$

where,

$$R_{in} = \left(\frac{1 - \mu}{\mu} \right)^2 R_L \quad (17)$$

and,

$$R_{out} = \frac{V_{mpp}^2}{P_{mpp}} \quad (18)$$

where V_{mpp} is the voltage corresponding to the MPP and P_{mpp} is the corresponding maximum power.

2.3 Mathematical modeling of single-phase H-bridge inverter

The H-bridge inverter with an LC filter has the capability to convert direct voltage to alternating voltage with minimal harmonic distortion and good frequency and amplitude stability across a range of resistive load values. Fig 8 displays a PWM inverter cascaded with the LC filter in standalone mode with a RIBSC. The inverter device consists of two basic elements: the power components and the device control unit [30].

The power component includes the following:

1. An H-bridge inverter typically composed of four electrical MOSFETs.

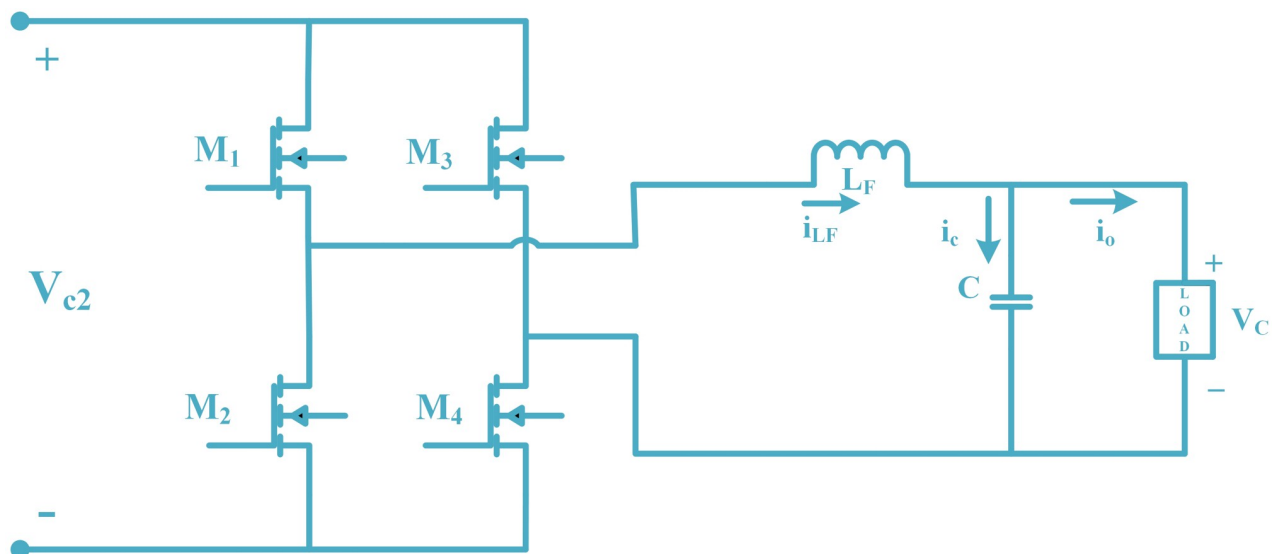


Fig 8. Basic diagram of a single-phase H-bridge inverter with LC filter.

<https://doi.org/10.1371/journal.pone.0297612.g008>

2. The LC filter, essential for obtaining a sine wave with appropriate recursion and minimizing output voltage distortion.

The second part consists of a controller, which is RIBSC. The RIBSC control law is derived in the next section. V_{c2} is the DC voltage, V_c is the output voltage after filtering, i_{LF} is the current of the inductor L_F , and i_o is the load current. The switching frequency applied to the electronic switch, which is 20 kHz, must be greater than the system frequency, which is 50 Hz, to obtain a reasonable inverter output voltage. Therefore, the Root Mean Square (RMS) of current and voltage are used. There are two modes for switching.

The state-space equation for when switches M1 and M4 are ON and M2 and M3 are OFF is as follows:

$$\begin{bmatrix} \frac{d}{dt} V_c \\ \frac{d}{dt} i_{LF} \\ \frac{d}{dt} V_{c2} \end{bmatrix} = \begin{bmatrix} 0 & \frac{1}{C} & 0 \\ -\frac{1}{L_F} & 0 & \frac{1}{L_F} \\ 0 & 0 & 0 \end{bmatrix} \begin{bmatrix} V_c \\ i_{LF} \\ V_{c2} \end{bmatrix} + \begin{bmatrix} -\frac{i_o}{C} \\ 0 \\ 0 \end{bmatrix} \tag{19}$$

The state-space equation for when switches M1 and M4 are OFF and M2 and M3 are ON is as follows:

$$\begin{bmatrix} \frac{d}{dt} V_c \\ \frac{d}{dt} i_{LF} \\ \frac{d}{dt} V_{c2} \end{bmatrix} = \begin{bmatrix} 0 & \frac{1}{C} & 0 \\ -\frac{1}{L_F} & 0 & -\frac{1}{L_F} \\ 0 & 0 & 0 \end{bmatrix} \begin{bmatrix} V_c \\ i_{LF} \\ V_{c2} \end{bmatrix} + \begin{bmatrix} -\frac{i_o}{C} \\ 0 \\ 0 \end{bmatrix} \tag{20}$$

Now, the average model for an H-bridge single-phase inverter in vector-matrix form is as:

$$\begin{bmatrix} \frac{d}{dt} V_c \\ \frac{d}{dt} i_{LF} \\ \frac{d}{dt} V_{c2} \end{bmatrix} = \begin{bmatrix} 0 & \frac{1}{C} & 0 \\ -\frac{1}{L_F} & 0 & \frac{\mu_2}{L_F} \\ 0 & 0 & 0 \end{bmatrix} \begin{bmatrix} V_c \\ i_{LF} \\ V_{c2} \end{bmatrix} + \begin{bmatrix} -\frac{i_o}{C} \\ 0 \\ 0 \end{bmatrix} \tag{21}$$

Taking into account the average value of V_c , i_{LF} , and V_{c2} , represented as x_1 , x_2 , and x_3 . Additionally, μ_2 is the inverter control law.

$$\begin{bmatrix} \dot{x}_1 \\ \dot{x}_2 \\ \dot{x}_3 \end{bmatrix} = \begin{bmatrix} 0 & \frac{1}{C} & 0 \\ -\frac{1}{L_F} & 0 & \frac{\mu_2}{L_F} \\ 0 & 0 & 0 \end{bmatrix} \begin{bmatrix} x_1 \\ x_2 \\ x_3 \end{bmatrix} + \begin{bmatrix} -\frac{i_o}{C} \\ 0 \\ 0 \end{bmatrix} \tag{22}$$

Representation from matrix shape to equation form is as follows:

$$\dot{x}_1 = \frac{x_2}{C} - \frac{i_o}{C} \tag{23}$$

$$\dot{x}_2 = -\frac{x_1}{L_F} + \frac{x_3 \mu_2}{L_F} \tag{24}$$

$$\dot{x}_3 = 0 \tag{25}$$

2.4 Reference voltage generation by regression plane

The PV characteristic curve changes with each specific estimation of irradiance and temperature. Even a slight change in either of them results in a new curve, subsequently altering the MPP, as depicted in Figs 5 and 6 [34]. By consistently changing temperature from 15°C to 35°C while maintaining a constant irradiance level of 1000 W/m², different MPPs have been recorded. Furthermore, by using linear regression at a constant temperature of 25 degrees Celsius, additional data points have been collected for irradiance levels ranging from 600 W/m² to 1400 W/m², resulting in a three-dimensional plane, as shown in Fig 9. Subsequently, for any temperature and irradiance level, a reference voltage (V_{PVref}) can be calculated as follows.

$$V_{PVref} = 579.81 - 1.9899 * T - 0.12146 * I \quad (26)$$

Where I is the irradiance and T is the temperature.

3. Proposed control algorithms

3.1 Control law for buck-boost converter using robust integral back-stepping controller

The primary objective of the control law is to attain MPP at the PV panel's output by continuously adjusting the duty cycle (μ) of the buck-boost converter. This goal is accomplished through a robust integral back-stepping control law, which drives the converter's output to track the reference (V_{PVref}) generated by the regression plane using linear interpolation. To design and implement a robust integral back-stepping control method [46] and to stabilize the buck-boost control action at the origin region (zero error), we need to define an error (e_1). This error is defined to enforce the input PV voltage V_{PV} to follow the regression plane's reference voltage (V_{PVref}) to track the MPP, as shown in Eq (27).

$$e_1 = x_1 - V_{PVref} \quad (27)$$

where (V_{PVref}) is the reference voltage, and x_1 is the input PV voltage. When e_1 is set to zero, we get the expected results. Taking the derivative of Eq (27) and substituting the dynamic

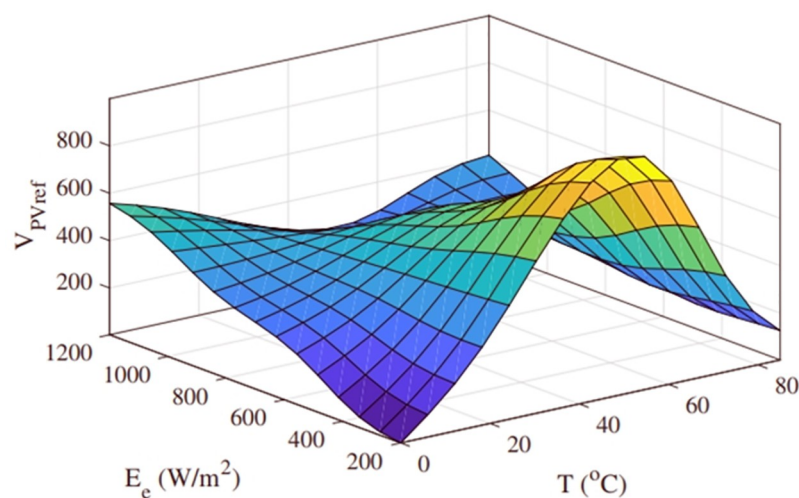


Fig 9. Regression plane.

<https://doi.org/10.1371/journal.pone.0297612.g009>

model equation mentioned in Eq (13), we get:

$$\dot{e}_1 = \frac{i_{pV}}{C_1} - \frac{\mu x_2}{C_1} - \dot{V}_{pVref} \tag{28}$$

The variable x_2 behaves as a virtual control input in Eq (28). Subsequently, a Lyapunov function is selected. For all x , it must be radially unbounded and positive definite, and its time derivative must be negative definite for all x to ensure a local asymptotically stable solution [47]. The selected function and its time derivative along with Eq (28) are as follows:

$$V_1 = \frac{1}{2}e_1^2 \tag{29}$$

$$\dot{V}_1 = e_1\dot{e}_1 = e_1 \left(\frac{i_{pV}}{C_1} - \frac{\mu x_2}{C_1} - \dot{V}_{pVref} \right) \tag{30}$$

To ensure \dot{V}_1 is negative, We substituted $-K_1e_1 - K_2\text{sign}(e_1)$ in the parenthesis term in Eq (30). Now, x_2 becomes:

$$x_2 = \left(K_1e_1 + \frac{i_{pV}}{C_1} - \dot{V}_{pVref} + K_2\text{sign}(e_1) \right) \frac{C_1}{\mu} \tag{31}$$

Using the value of x_2 from Eq (31), Eq (30) becomes,

$$\dot{V}_1 = -K_1e_1^2 - K_2e_1\text{sign}(e_1) \tag{32}$$

Eq (32) shows that for the Lyapunov function derivative to be negative definite, it is necessary that K_1 and K_2 must be positive, and Eq (31) must also be satisfied. Now, for x_2 , the inductor current needs a reference current denoted as α , serving as a stabilizing function. Additionally, the term $\lambda\theta$ is added for robustness, which represents the integral action term where θ is equal to the integral of e_1 .

$$\alpha = \left(C_1K_1e_1 + i_{pV} - C_1\dot{V}_{pVref} + K_2C_1\text{sign}(e_1) \right) \frac{1}{\mu} + \lambda\theta \tag{33}$$

Now, the reference current α follows the inductor current x_2 , and e_2 must be zero.

$$e_2 = x_2 - \alpha \tag{34}$$

or,

$$x_2 = e_2 + \alpha \tag{35}$$

Putting Eq (35) in Eq (28), we get:

$$\dot{e}_1 = -K_1e_1 - K_2\text{sign}(e_1) - \frac{\mu e_2}{C_1} \tag{36}$$

Now, using Eq (36), Eq (30) becomes,

$$\dot{V}_1 = -K_1e_1^2 - K_2e_1\text{sign}(e_1) - \frac{\mu e_1e_2}{C_1} \tag{37}$$

Now, take the derivate of the second error, as defined in Eq (34),

$$\dot{e}_2 = \dot{x}_2 - \dot{\alpha} \tag{38}$$

Also differentiate Eq (33) w.r.t time,

$$\dot{\alpha} = \frac{1}{\mu^2} \left((K_1 \dot{e}_1 C_1 + \dot{i}_{pV} - \ddot{V}_{pVref} C_1) \mu - (K_1 e_1 C_1 + i_{pV} - C_1 \dot{V}_{pVref} + K_2 C_1 \text{sign}(e_1)) \dot{\mu} \right) + \lambda e_1 \quad (39)$$

Putting Eq (36) in the above equation, we get:

$$\begin{aligned} \dot{\alpha} &= \frac{1}{\mu} \left(-K_1^2 e_1 C_1 - K_1 K_2 C_1 \text{sign}(e_1) + i_{pV} - \ddot{V}_{pVref} C_1 \right) \mu \\ &\quad - \frac{\alpha \dot{\mu}}{\mu} - K_1 e_2 + \lambda e_1 \end{aligned} \quad (40)$$

Substituting Eqs (14) and (40) in Eq (38), we get:

$$\dot{e}_2 = -\frac{x_3}{L} + \mu \frac{x_1 + x_3}{L} - \frac{1}{\mu} \left(-K_1^2 e_1 C_1 - K_1 K_2 C_1 \text{sign}(e_1) + i_{pV} - \ddot{V}_{pVref} C_1 \right) + \frac{\alpha \dot{\mu}}{\mu} + K_1 e_2 - \lambda e_1 \quad (41)$$

Now, to ensure system asymptotic stability and the convergence of error e_1 and error e_2 to zero, we check the Lyapunov composite function for this system.

$$V_2 = V_1 + \frac{1}{2} e_2^2 \quad (42)$$

The time derivative of the above equation along with Eq (37) is,

$$\dot{V}_2 = \dot{V}_1 + e_2 \dot{e}_2 = -K_1 e_1^2 - K_2 e_1 \text{sign}(e_1) + e_2 \left(\dot{e}_2 - \mu \frac{e_1}{C_1} \right) \quad (43)$$

For the Lyapunov function derivative to be negative we substitute parenthesis term of Eq (37) to $-K_3 e_2 - K_4 \text{sign}(e_2)$, and we get,

$$\dot{e}_2 - \mu \frac{e_1}{C_1} = -K_3 e_2 - K_4 \text{sign}(e_2) \quad (44)$$

K_3 and K_4 must be positive definite. Put Eq (41) in Eq (44),

$$\begin{aligned} -K_3 e_2 - K_4 \text{sign}(e_2) &= -\frac{x_3}{L} + \mu \frac{x_1 + x_3}{L} - \frac{1}{\mu} \left(-K_1^2 e_1 C_1 - K_1 K_2 C_1 \text{sign}(e_1) + i_{pV} - \ddot{V}_{pVref} C_1 \right) + \frac{\alpha \dot{\mu}}{\mu} + K_1 e_2 - \lambda e_1 \\ &\quad - \mu \frac{e_1}{C_1} \end{aligned} \quad (45)$$

Solving for $\dot{\mu}$ the final expression for control law is shown in Eq (46),

$$\begin{aligned} \dot{\mu} &= \frac{1}{\alpha} \left[e_2 (-K_1 - K_3) \mu - e_1 \left(C_1 K_1^2 - \frac{\mu^2}{C_1} - \mu \lambda \right) + \mu \frac{x_3}{L} \right] + \\ &\quad \frac{1}{\alpha} \left[\dot{i}_{pV} - C_1 \ddot{V}_{pVref} - \mu^2 \left(\frac{x_1 + x_3}{L} \right) - K_1 K_2 C_1 \text{sign}(e_1) \right] + \\ &\quad \frac{\mu}{\alpha} [-K_4 \text{sign}(e_2)] \end{aligned} \quad (46)$$

Where $\alpha \neq 0$ and $0 < \mu < 1$.

Eq (46) shows the control law for a buck-boost converter using a robust integral back-stepping controller.

3.2 Control law for inverter using robust integral back-stepping controller

The objective is to use a Robust Integral Back-Stepping Controller (RIBSC) to generate a sinusoidal output voltage at the load terminal, facilitating closed-loop control. The RIBSC structure is primarily based on the Lyapunov dynamic system stability theory [48]. This process is intended to force the inverter output voltage x_1 closely track reference voltage U_{cref} with the highest degree of robustness and minimal THD. Therefore, e_3 represents the error, defined in Eq (47).

$$e_3 = U_{cref} - x_1 \tag{47}$$

The goal is to get e_3 close to zero. Taking the derivative of Eq (47) and substituting the dynamic model equation described in Eq (23), we get:

$$\dot{e}_3 = \dot{U}_{cref} - \frac{x_2}{C} + \frac{i_o}{C} \tag{48}$$

Choosing a Lyapunov function, and the time derivative of the Lyapunov function along with Eq (48) is as follows:

$$V_1 = \frac{1}{2}e_3^2 \tag{49}$$

$$\dot{V}_1 = e_3\dot{e}_3 = e_3\left(\dot{U}_{cref} - \frac{x_2}{C} + \frac{i_o}{C}\right) \tag{50}$$

Second error is defined as follows,

$$e_4 = \alpha - x_2 \tag{51}$$

or,

$$x_2 = \alpha - e_4 \tag{52}$$

So, the derivative of Eq (51) is,

$$\dot{e}_4 = \dot{\alpha} - \dot{x}_2 \tag{53}$$

Putting Eq (24) in Eq (53), we get:

$$\dot{e}_4 = \dot{\alpha} + \frac{x_1}{L_F} - \frac{\mu_2 V_{c2}}{L_F} \tag{54}$$

From Eq (50), substituting $-K_3e_3 - K_4\text{sign}(e_3)$ for robustness,

$$x_2 = C\dot{U}_{cref} + K_3e_3C + i_o + CK_4\text{sign}(e_3) \tag{55}$$

For V_1 to be negative definite, K_3 and K_4 must be positive definite, and Eq (55) must satisfy α . Additionally, the term $\lambda\theta$ is added for robustness, representing the integral action term where θ is equal to the integral of e_3 . So,

$$\alpha = (C\dot{U}_{cref} + K_3e_3C + i_o + CK_4\text{sign}(e_3)) + \lambda\theta \tag{56}$$

Putting Eq (52) in Eq (50), we get:

$$\dot{V}_1 = e_3\left(\dot{U}_{cref} - \frac{\alpha}{C} + \frac{i_o}{C} + \frac{e_4}{C}\right) \tag{57}$$

Putting the value of α into the above equation, we get:

$$\dot{V}_1 = -K_3 e_3^2 + \frac{e_3 e_4}{C} - K_4 e_3 \text{sign}(e_3) \tag{58}$$

Taking the derivative of Eq (56) and its simplified form is as follows,

$$\dot{\alpha} = C\ddot{U}_{cref} + K_3 \dot{e}_3 C + i_o + 0 + \lambda e_3 \tag{59}$$

$$\dot{\alpha} = C\ddot{U}_{cref} - K_3^2 e_3 C - CK_4 K_3 \text{sign}(e_3) + i_o + \lambda e_3 \tag{60}$$

Choosing a second Lyapunov function,

$$V_2 = V_1 + \frac{1}{2} e_4^2 \tag{61}$$

Its derivative along Eq (58) is,

$$\dot{V}_2 = \dot{V}_1 + e_4 \dot{e}_4 = -K_3 e_3^2 - K_4 e_3 \text{sign}(e_3) + e_4 \left(\frac{e_3}{C} + \dot{e}_4 \right) \tag{62}$$

Putting Eq (54) in Eq (62), we get:

$$\dot{V}_2 = -K_3 e_3^2 - K_4 e_3 \text{sign}(e_3) + e_4 \left(\frac{e_3}{C} + \dot{\alpha} - \frac{\mu_2 V_{c2}}{L_F} + \frac{x_1}{L_F} \right) \tag{63}$$

Putting Eq (60) in Eq (63), we get:

$$\dot{V}_2 = -K_3 e_3^2 - \frac{K_4 e_3 \text{sign}(e_3)}{C} + e_4 \left(\frac{e_3}{C} + C\ddot{U}_{cref} - K_3^2 e_3 C - CK_4 K_3 \text{sign}(e_3) + i_o + \lambda e_3 - \frac{\mu_2 V_{c2}}{L_F} + \frac{x_1}{L_F} \right) \tag{64}$$

$$\begin{aligned} & \frac{e_3}{C} + C\ddot{U}_{cref} - K_3^2 e_3 C - CK_4 K_3 \text{sign}(e_3) + i_o + \lambda e_3 - \frac{\mu_2 V_{c2}}{L_F} \\ & + \frac{x_1}{L_F} = -K_5 e_4 - K_6 \text{sign}(e_4) \end{aligned} \tag{65}$$

To get $\dot{V}_2 < 0$ a control law μ_2 is chosen from the inverter defined in Eq (66),

$$\mu_2 = \frac{L_F}{V_{c2}} \left(\frac{e_3}{C} + C\ddot{U}_{cref} - K_3^2 e_3 C - CK_4 K_3 \text{sign}(e_3) + i_o + \lambda e_3 + \frac{x_1}{L_F} + K_5 e_4 + K_6 \text{sign}(e_4) \right) \tag{66}$$

The error e_3 tends to zero with the application of this control rule to the PWM inverter in the standalone mode because the derivative of V_1 and V_2 is negative.

4. Simulation results

To analyze the overall performance of the PV system with the inverter using the proposed technique, MATLAB/Simulink is used. The system parameters are listed in Table 1, and the controller parameters can be found in Table 2. The proposed technique is evaluated in two different scenarios: 1) Steady-state performance of the inverter output voltage with different loads 2) Transient performance of the inverter output voltage with different loads when the reference amplitude changes in steps. The performance of the proposed technique is analyzed and compared with the back-stepping and PID controllers.

Table 1. System parameters.

Types	Parameter	Symbol	Value	Unit
PV module	Maximum power	P_{max}	1555	W
	Number of cells per module	N_s	72	
	Voltage at maximum power	V_{mp}	102.6	V
	Open circuit voltage	V_{oc}	165.8	V
	Short circuit current	I_{sc}	17.56	A
	Current at maximum power	I_{mp}	15.16	A
Converter	Converter input capacitor	C_1	1	mF
	Converter output capacitor	C_2	48	μ F
	Converter inductor	L	20	mH
	Switching frequency	f_s	5	kHz
Inverter and LC filter	Inductor	L_F	47	mH
	capacitor	C	150	μ F
	Switching frequency	f_s	20	kHz

<https://doi.org/10.1371/journal.pone.0297612.t001>

4.1 Steady-state performance of the inverter output voltage with different loads

Fig 10 illustrates the profile of varying temperature and irradiance. The temperature is initially held at 25°C, and the irradiance at 650 W/m² from 0s to 0.1s. Between 0.1s and 0.2s, the temperature changes to 65°C, and the irradiance to 1000 W/m². In the subsequent time interval, the temperature is reverted to 25°C, and the irradiance to 650 W/m². The reference voltage, generated through the regression plane, is successfully tracked by the PV array output voltage, as shown in Fig 11. It is evident from the results that the RIBSC controller reaches a steady-state condition in less than 0.15s compared to other benchmark controllers. PV module output power under fluctuating environmental conditions are shown in Fig 12. The output power is 18.4kW from 0.1s to 0.2s, 19.02kW for the second interval, and the same as the first interval for the last interval. The performance criteria (i.e. ITSE, ITAE, ISE, and IAE, where the error here is the difference between the reference power and the output power of PV array) assesses the robustness of the proposed controller. Fig 13 shows that the proposed controller accumulates less error compared to the back-stepping controller. The formulas for calculating these

Table 2. Controllers parameters.

Type	Controllers Constant Parameter	Symbol	Value
Converter RIBSC	Constant	K_1	100
	Constant	K_2	9000
	Constant	K_3	2000
	Constant	K_4	10
	Constant	λ	29
Inverter RIBSC	Constant	K_3	70000
	Constant	K_4	20000
	Constant	K_5	70000
	Constant	K_6	20000
	Constant	λ	100

<https://doi.org/10.1371/journal.pone.0297612.t002>

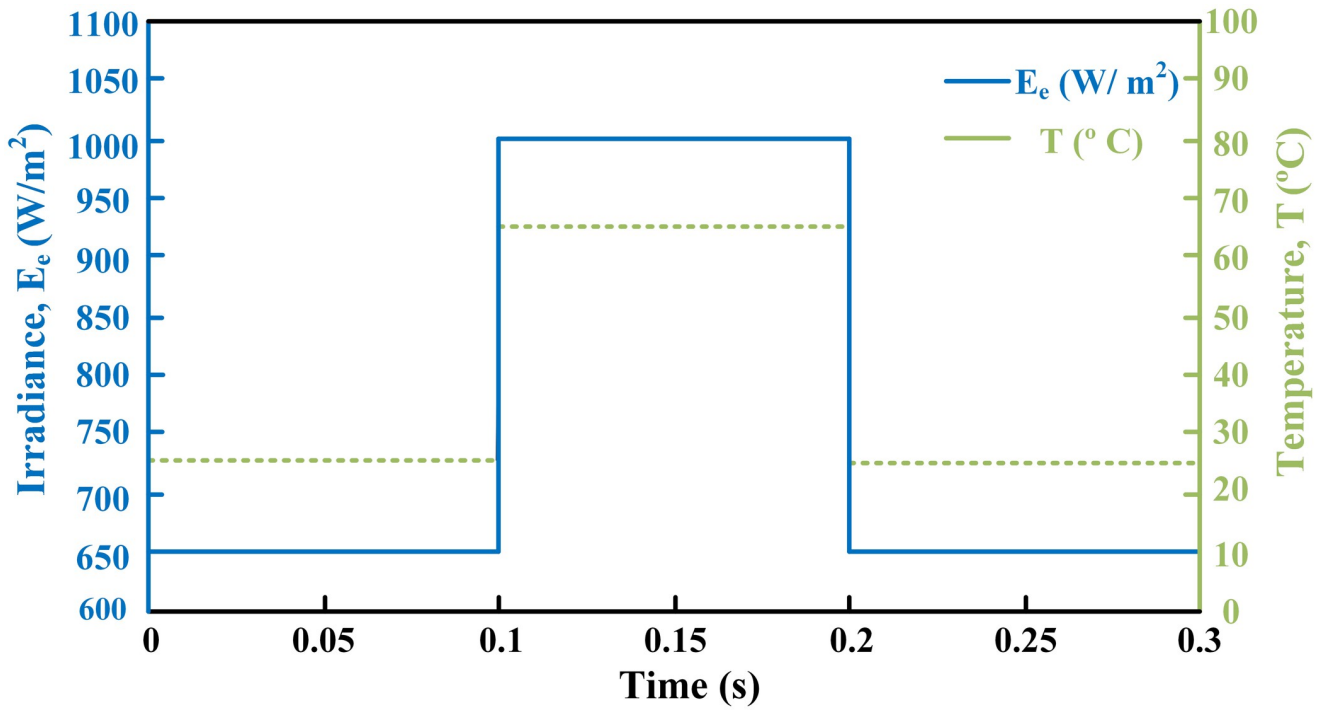


Fig 10. Varying temperature and irradiance profile.

<https://doi.org/10.1371/journal.pone.0297612.g010>

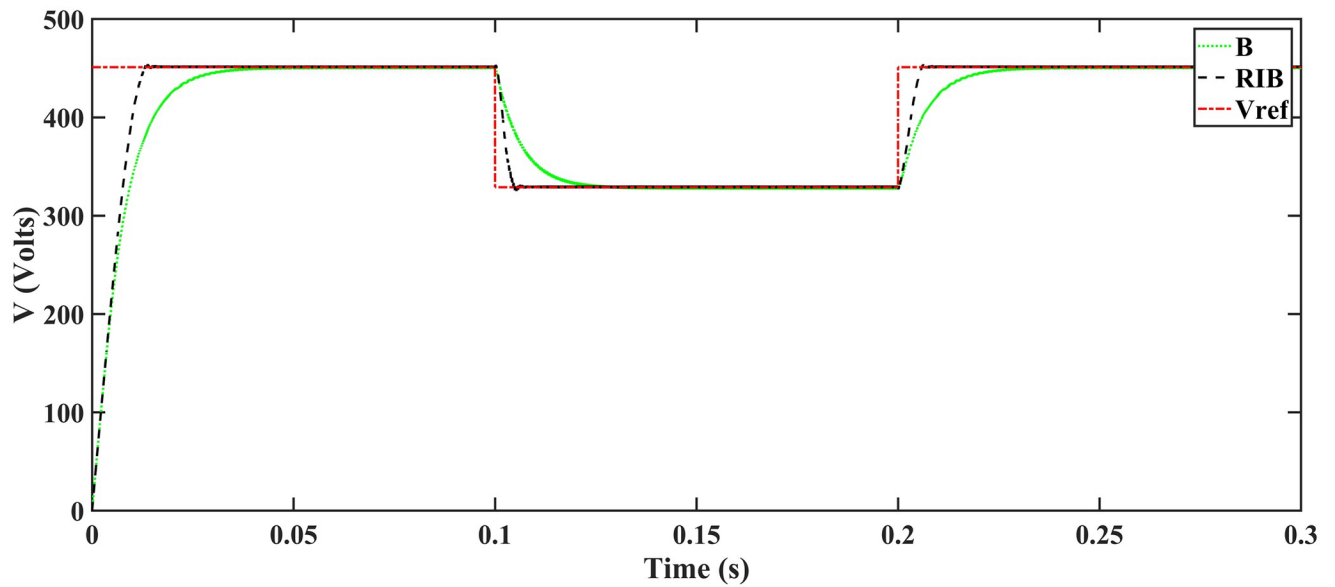


Fig 11. Output voltage of the PV array.

<https://doi.org/10.1371/journal.pone.0297612.g011>

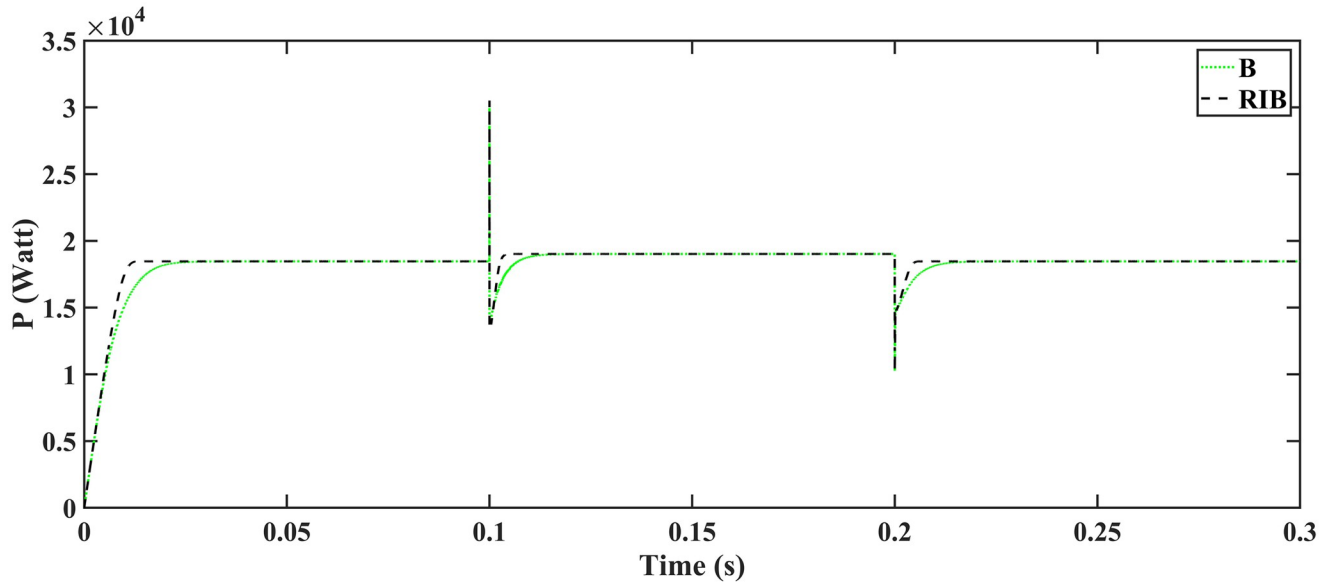


Fig 12. Output power of the PV array.

<https://doi.org/10.1371/journal.pone.0297612.g012>

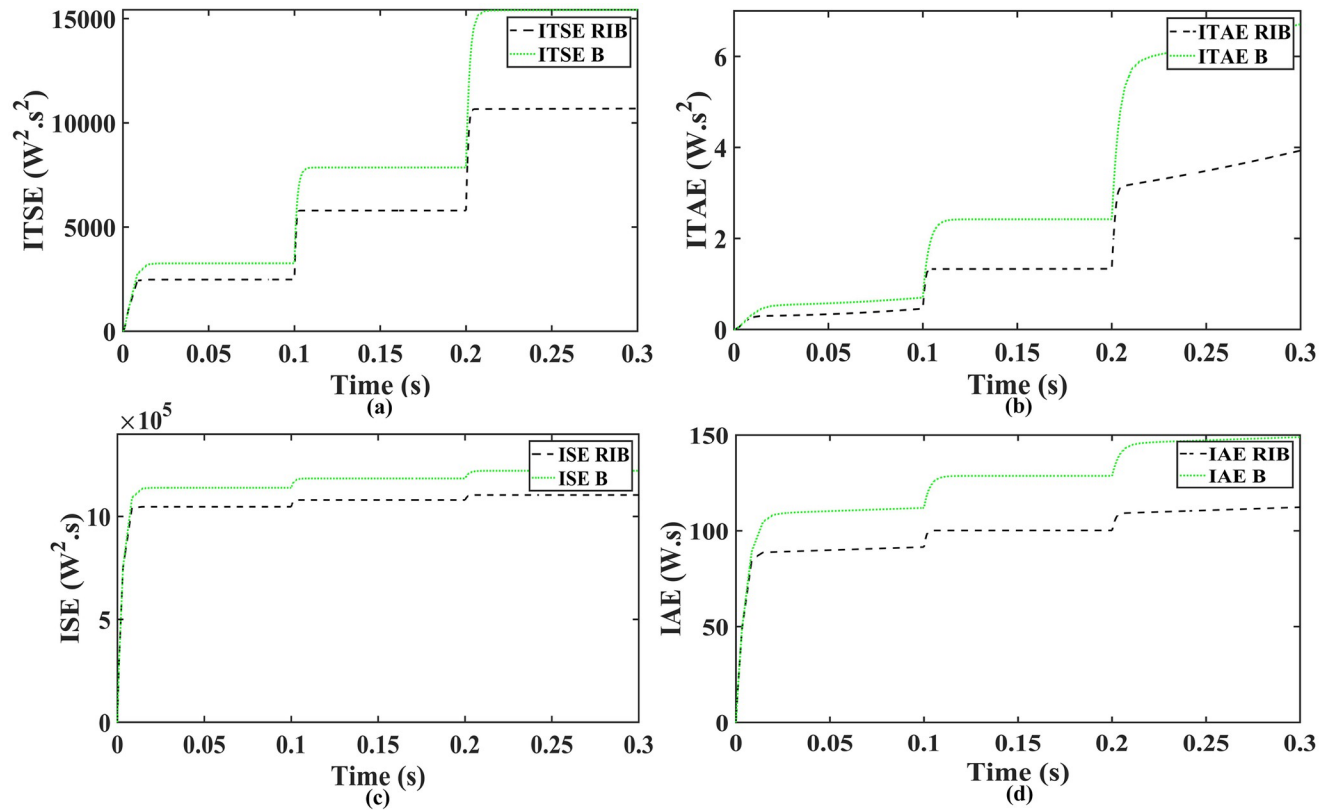


Fig 13. Performance indices of PV array output power (a)ITSE (b)ITAE (c)ISE (d)IAE.

<https://doi.org/10.1371/journal.pone.0297612.g013>

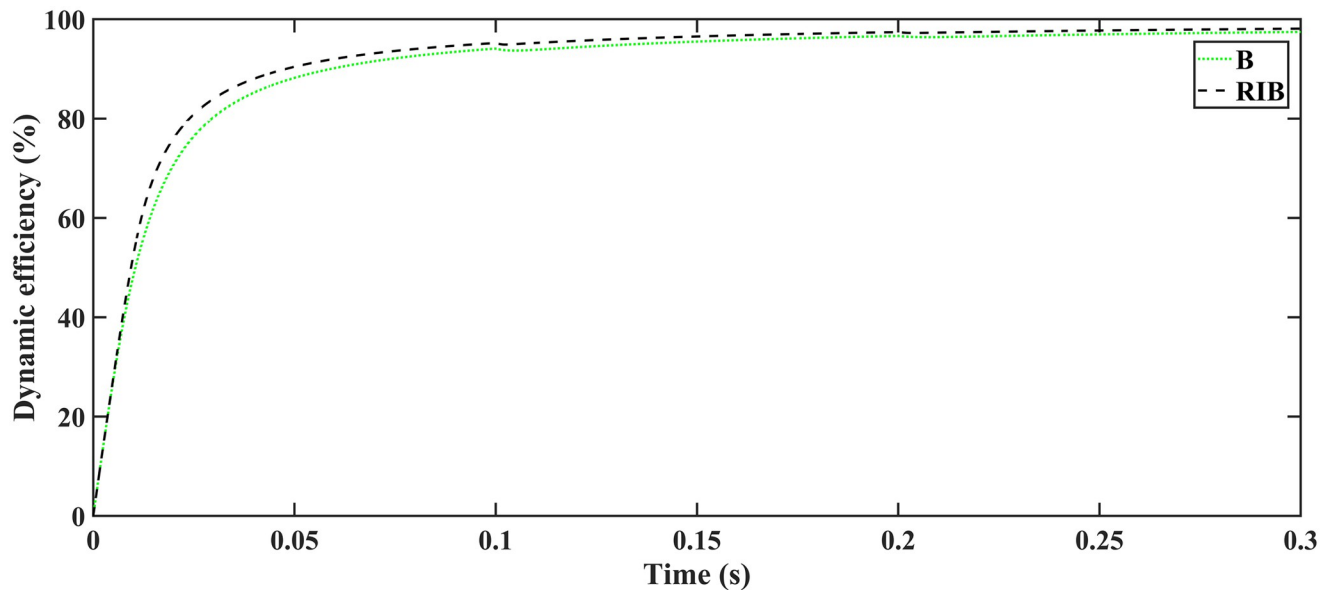


Fig 14. Dynamic efficiency.

<https://doi.org/10.1371/journal.pone.0297612.g014>

errors are as follows:

$$ITSE = \int_{t_0}^{t_f} te(t)^2 dt \tag{67}$$

$$ITAE = \int_{t_0}^{t_f} t|e(t)|dt \tag{68}$$

$$ISE = \int_{t_0}^{t_f} e(t)^2 dt \tag{69}$$

$$IAE = \int_{t_0}^{t_f} |e(t)|dt \tag{70}$$

The dynamic efficiency of back-stepping is 97.45%, while for robust integral back-stepping, it is 98.11% at the MPPT stage, as shown in Fig 14. The efficiency of MPPT controller is compared with other state-of-the-art techniques in Table 3. Dynamic efficiency is defined as the ratio of PV output power to the PV power at MPP over a specific time period, and it is defined

Table 3. MPPT dynamic efficiency.

Algorithms	Efficiency (%)
P & O	96
PI	96.5
Back-stepping	97.45
Robust integral back-stepping (Proposed)	98.11

<https://doi.org/10.1371/journal.pone.0297612.t003>

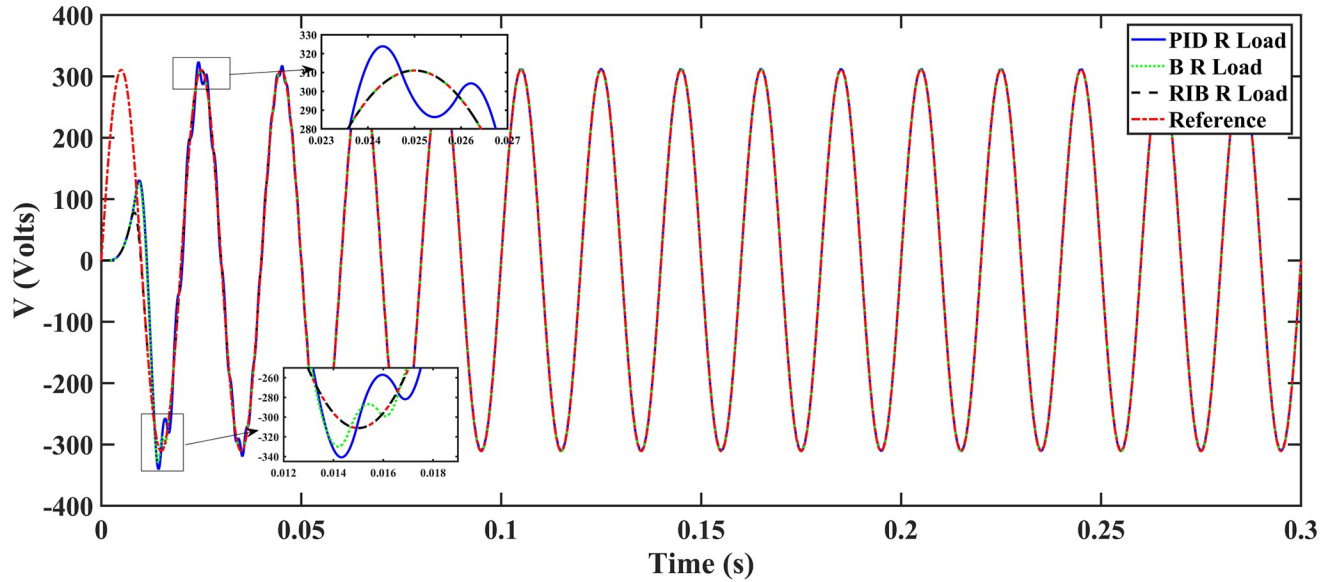


Fig 15. Inverter output voltage at resistive load after filtering.

<https://doi.org/10.1371/journal.pone.0297612.g015>

as;

$$\eta_{100} = \frac{\int_{t_0}^{t_f} P_{PV} dt}{\int_{t_0}^{t_f} P_{MPP} dt} \times 100 = \frac{\int_{t_0}^{t_f} (V_{PV} \times I_{PV}) dt}{\int_{t_0}^{t_f} P_{MPP} dt} \times 100 \tag{71}$$

Because of the robustness, we use robust integral back-stepping for all scenarios. The MPPT is unaffected and remains the same for all loads.

4.1.1 Scenario 1. In scenario 1, a resistive load is considered, and the inverter’s performance with different controllers are depicted in Fig 15. The plot depicts four wave-forms: the inverter’s output voltage at the load terminal V_C for three controllers and the sinusoidal reference signal U_{cref} . The results show that the output voltage perfectly tracks the reference voltage, which is a sinusoidal waveform. The proposed controller tracks the reference voltage in almost 0.01s, while the back-stepping and PID controllers do so in 0.025s and 0.04s, respectively. As can be seen from Fig 15, the initial response of PID and back-stepping controllers have overshoots and undershoots, whereas the proposed controller has readily tracked the reference voltage from the start without any overshoot and undershoot. This also implies the convergence time of the proposed controller is smaller. When the inverter’s input voltage is below 700V which is the nominal input voltage of the inverter, a drop appears in the output voltage. The distortion in the output voltage at the beginning is due to the insufficient voltage provided by the non-inverting buck-boost converter. After 0.01s, in the case of the proposed controller, the input voltage of the inverter exceeds 700V and the output voltage of the inverter begins to track the reference voltage. The frequency analysis of the output voltage and Root Means Square Error (RMSE) are compared in Tables 4 and 5, respectively. RMSE is a commonly used measure for evaluating the quality of actual values, indicating how far the actual values deviate from the true measured values. To compute RMSE, the residual (the difference between

Table 4. Comparison of THD of different control techniques.

Scenario	Normal Operation			Step changes in reference amplitude		
Control Techniques	Scenario 1 (%)	Scenario 2 (%)	Scenario 3 (%)	Scenario 4 (%)	Scenario 5 (%)	Scenario 6 (%)
PID	13.18	13.18	20.13	14.27	14.28	21.57
Back-stepping	12.66	12.66	14.22	13.82	13.82	15.76
Robust Integral Back-stepping	9.71	9.72	13.04	11.45	11.45	14.33

<https://doi.org/10.1371/journal.pone.0297612.t004>

Table 5. Root Means Square Error (RMSE) of reference voltage and output voltage of inverter.

Scenario	Normal Operation			Step changes in reference amplitude		
Control Techniques	Scenario 1	Scenario 2	Scenario 3	Scenario 4	Scenario 5	Scenario 6
PID	0.4523	0.4524	0.833	0.4529	0.4536	0.888
Back-stepping	0.4365	0.4365	0.586	0.4371	0.4371	0.6025
Robust Integral Back-stepping	0.3998	0.40	0.5477	0.408	0.409	0.5624

<https://doi.org/10.1371/journal.pone.0297612.t005>

prediction and truth) for each data point is calculated, norm of residuals for each data point are found, mean of residuals is computed, and then square root of the resulting mean is computed.

$$RMSE = \sqrt{\frac{\sum_{i=1}^N |V_{ref} - V_{out}|^2}{N}} \tag{72}$$

The fundamental voltage is about 300.8V, 301.3V, and 301.8V for the PID controller, back-stepping controller and proposed controller, respectively, at a frequency of 50Hz. The THD for these controllers is 13.18%, 12.66%, and 9.71%. THD measures the total amount of harmonic distortion present in a current signal and is expressed as a percentage, as follows

$$THD\% = \frac{\sqrt{\sum_{n=1}^{n=\max} I_n^2}}{I_0} \tag{73}$$

In this equation, I_0 represents the fundamental component of the signal, and I_n stands for the n th order harmonics of the same signal. The RIB controller exhibits a lower harmonic distortion compared to the benchmark controllers, which is less than 5% according to the IEEE standard. As is evident from Fig 16, the THD due to proposed controller converges to zero level earlier than the PID and back-stepping controllers. In other words, the proposed controller as fewer harmonics in the output of the inverter. The performance indices of the inverter output voltage is calculated in Fig 17 and are compared in Table 6. Fig 17 shows the tracking error in terms of four error metrics. As can be seen from the figures, PID controller has the largest error and the proposed controller has the minimum error. In addition, Fig 17(b) and 17(d) shows that the tracking error due to PID controller keeps on increasing and does not converge in finite time. The inverter, evaluated with the suggested controller in standalone mode, displays low harmonic distortion, strong control performance, and a high-quality sinusoidal waveform, as can be concluded from Figs 15–17.

4.1.2 Scenario 2. We assume resistive inductive loads in scenario 2. The performance of the inverter with different controllers are shown in Fig 18, depicting four wave-forms: the inverter’s output voltage at the terminal load V_C for the three controllers and the sinusoidal

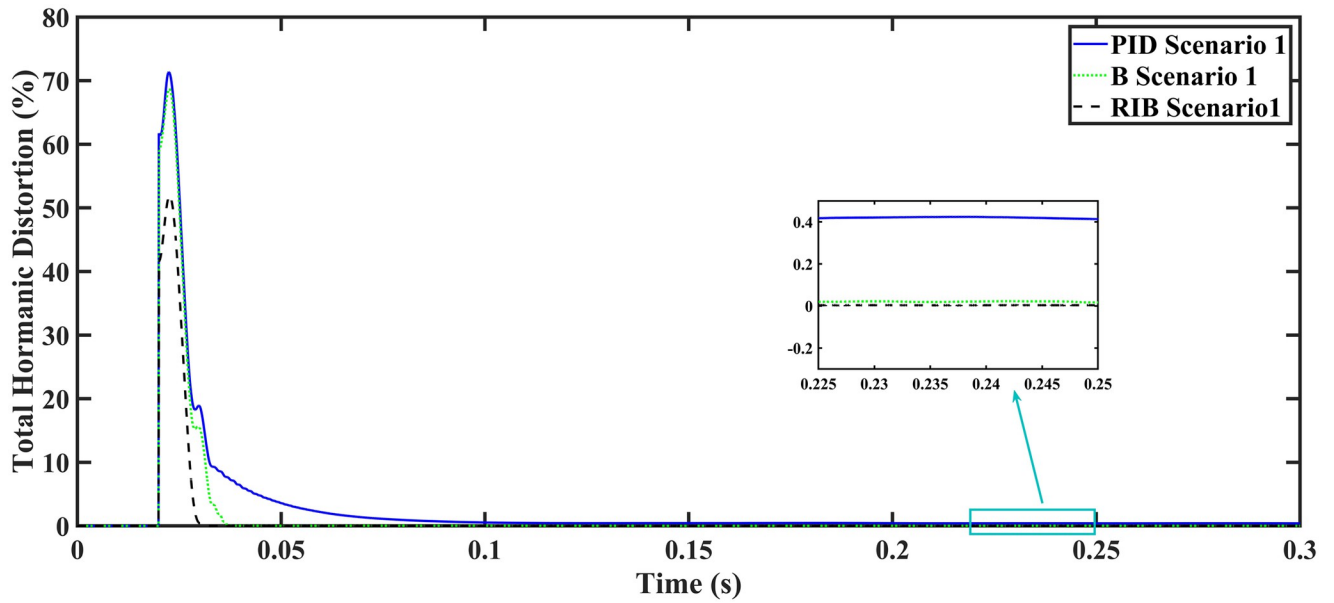


Fig 16. Total harmonic distortion.

<https://doi.org/10.1371/journal.pone.0297612.g016>

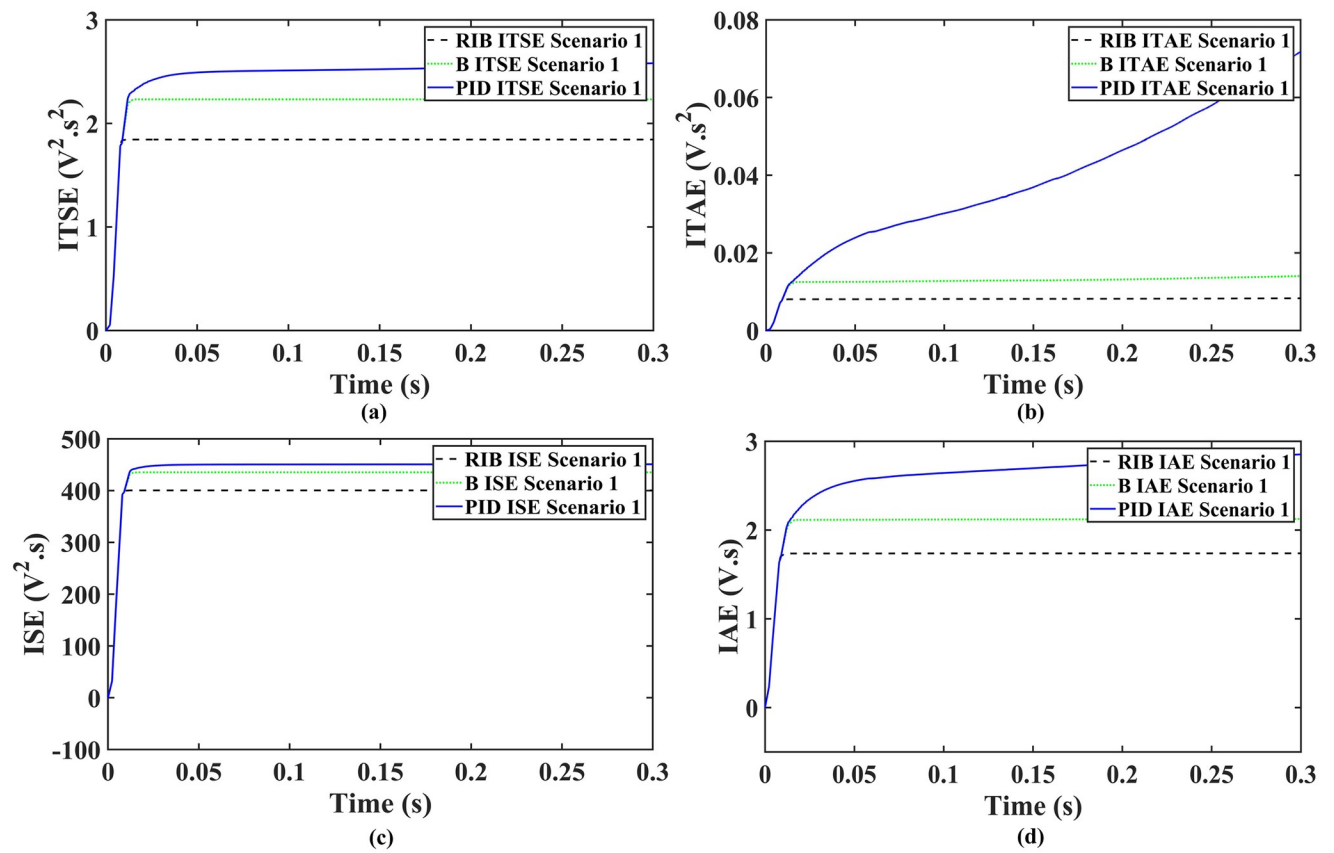


Fig 17. Performance indices of inverter output voltage with resistive load (a)ITSE (b)ITAE (c)ISE (d)IAE.

<https://doi.org/10.1371/journal.pone.0297612.g017>

Table 6. Comparison of ITSE, ITAE, ISE and IAE under normal operation.

Scenario	Scenario 1			Scenario 2			Scenario 3		
Control Techniques	PID	B	RIB	PID	B	RIB	PID	B	RIB
ITSE	2.581	2.232	1.844	2.594	2.242	1.855	38.12	4.622	3.962
ITAE	0.0718	0.0140	0.0081	0.0720	0.0139	0.0083	0.991	0.0992	0.0864
ISE	450.8	435.3	400.3	451.6	436	401	834.8	587.6	548.4
IAE	2.852	2.124	1.738	2.865	2.121	1.742	9.423	3.339	3.181

<https://doi.org/10.1371/journal.pone.0297612.t006>

reference signal U_{ref} . The results show that the output voltage perfectly tracks the reference voltage, which is a sinusoidal waveform. The proposed controller tracks the reference voltage in almost 0.01s, while the back-stepping controller and the PID controller track in 0.025s and 0.04s, respectively. As can be seen from Fig 18, the initial response of PID and back-stepping controllers have overshoots and undershoots, whereas the proposed controller has readily tracked the reference voltage from the start without any overshoot and undershoot. This also implies the convergence time of the proposed controller is smaller. If the inverter input voltage is less than 700V which is the nominal voltage of the inverter input, then a drop appears in the output voltage. The distortion in the output voltage of the inverter at the beginning is due to the insufficient voltage provided by the non-inverting buck-boost converter. After 0.01s, in the case of the proposed controller, the input voltage of the inverter exceeds 700V and the output voltage of the inverter begins to track the reference voltage. The output voltage frequency analysis and RMSE are compared in Tables 4 and 5, respectively. The fundamental voltage is about 300.8V, 301.3V, and 301.8V in the case of the PID controller, back-stepping controller, and proposed controller, respectively, at a 50Hz frequency, while the THD is 13.18%, 12.66%, and 9.72%. This means that the RMS magnitude of harmonic frequencies are 13.18%, 12.66%, and 9.72% of the RMS magnitude of the fundamental frequency. The RIB controller shows better harmonic distortion compared to the benchmark controllers, which is less than 5% according

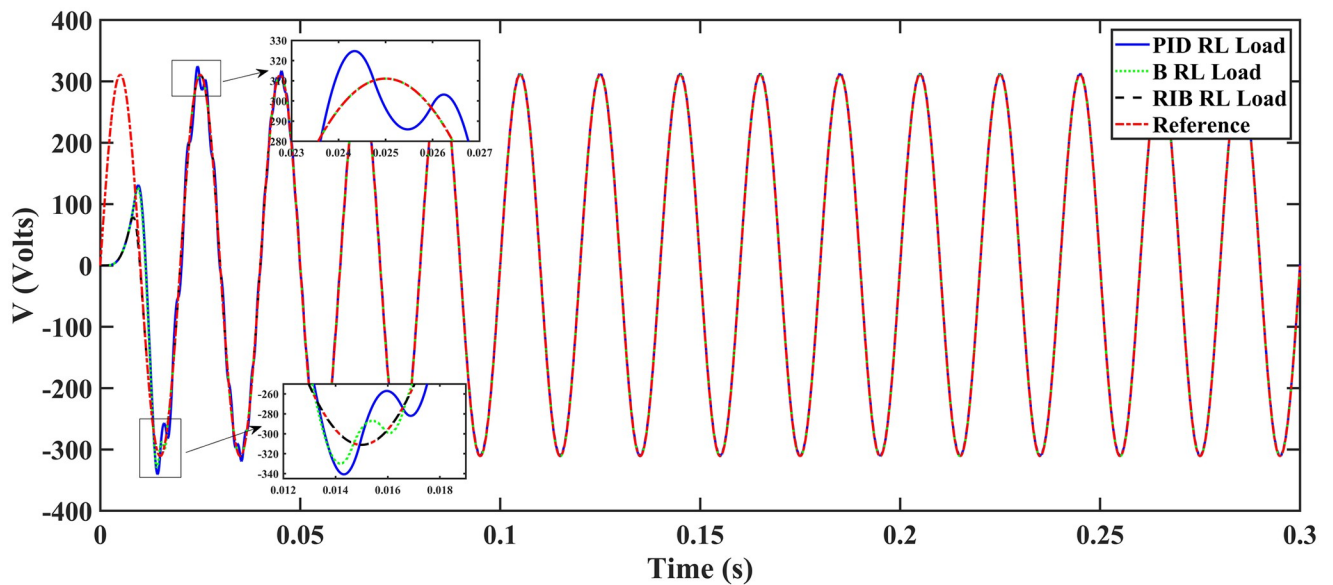


Fig 18. Inverter output voltage at resistive inductive loads after flirting.

<https://doi.org/10.1371/journal.pone.0297612.g018>

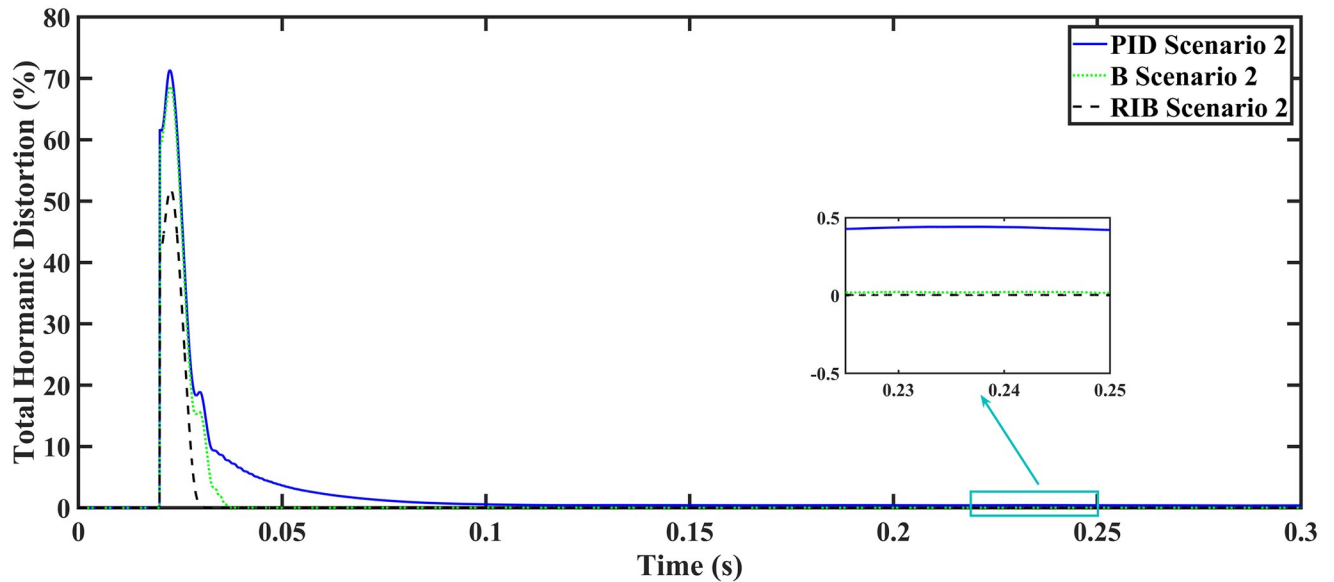


Fig 19. Total harmonic distortion.

<https://doi.org/10.1371/journal.pone.0297612.g019>

to the IEEE standard. As is evident from Fig 19, the THD due to proposed controller converges to zero level earlier than the PID and back-stepping controllers. In other words, the proposed controller as fewer harmonics in the output of the inverter. The performance indices of the inverter output voltage is calculated in Fig 20 and are compared in Table 6. Fig 20 shows the tracking error in terms of four error metrics. As can be seen from the figures, PID controller has the largest error and the proposed controller has the minimum error. In addition, Fig 17 (b) and 17(d) shows that the tracking error due to PID controller keeps on increasing and does not converge in finite time. The inverter, evaluated with the suggested controller in standalone mode, exhibits low harmonic distortion, strong control performance, and a high-quality sinusoidal waveform, as can be concluded from Figs 18–20.

4.1.3 Scenario 3. The resistive, inductive, and capacitive loads are employed in scenario 3. The performance of the inverter with different controllers are shown in Fig 21. This plot depicts four waveforms: the inverter's output voltage at the terminal load V_C for three controllers and the sinusoidal reference signal U_{ref} . This shows that the output current of the inverter does not affect the output voltage of the inverter. The results show that the output voltage perfectly tracks the reference voltage, which is a sinusoidal waveform. As can be seen from Fig 21, the initial response of PID and back-stepping controllers have overshoots and undershoots, whereas the proposed controller has readily tracked the reference voltage from the start without any overshoot and undershoot. This also implies the convergence time of the proposed controller is smaller. This means that the proposed controller tracks the reference voltage faster compared to the benchmark controllers. If the inverter input voltage is less than 700V which is the nominal voltage of the inverter input, then a drop appears at the output voltage. The distortion in the output voltage of the inverter at the beginning is due to insufficient voltage provided by the non-inverting buck-boost converter. After 0.01s, in the case of the proposed controller, the input voltage of the inverter exceeds 700V and the output voltage of the inverter begins to track the reference voltage. The output voltage frequency analysis and RMSE are compared in Tables 4 and 5, respectively. The fundamental voltage is about 295.9V, 297.2V, and 294.9V in the case of the PID controller, back-stepping controller, and proposed

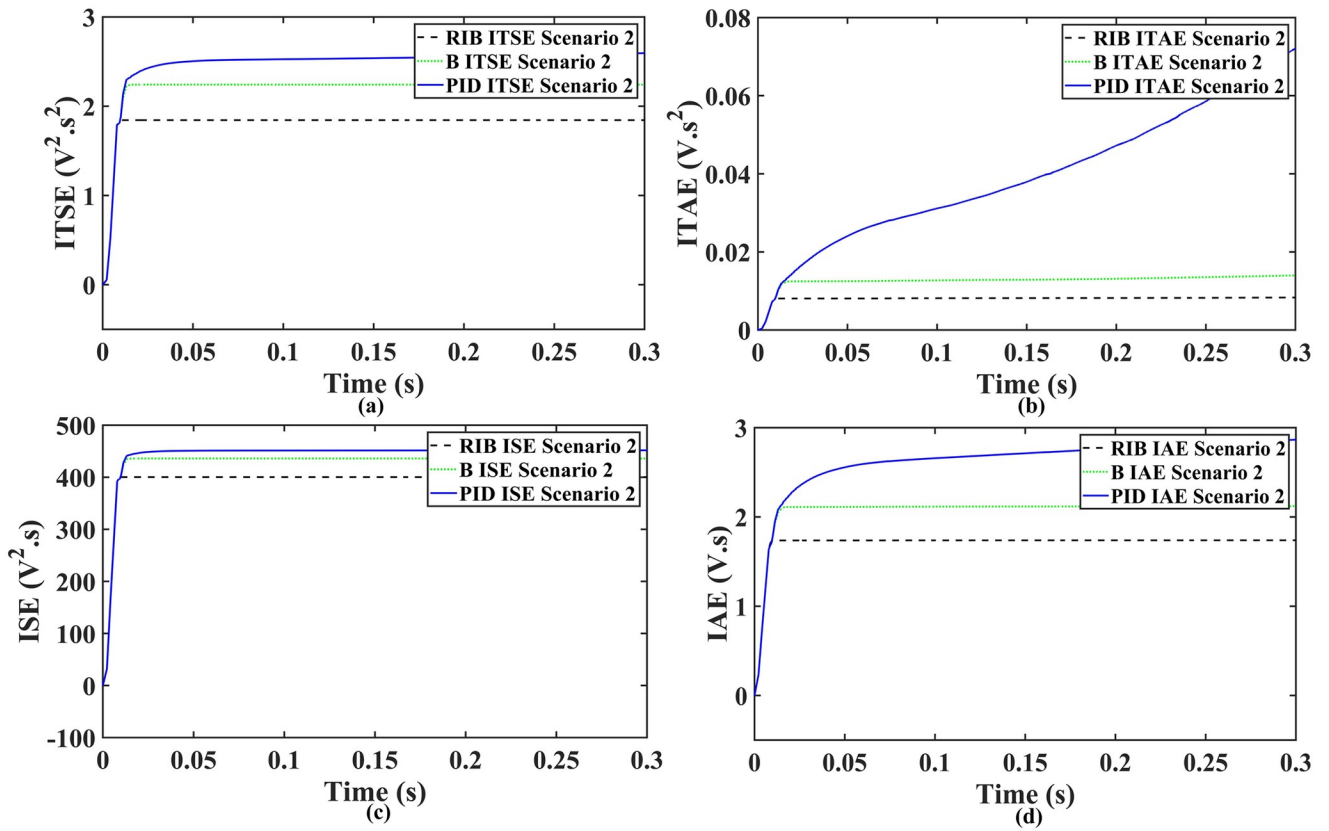


Fig 20. Performance indices of inverter output voltage with resistive inductive loads (a)ITSE (b)ITAE (c)ISE (d)IAE.

<https://doi.org/10.1371/journal.pone.0297612.g020>

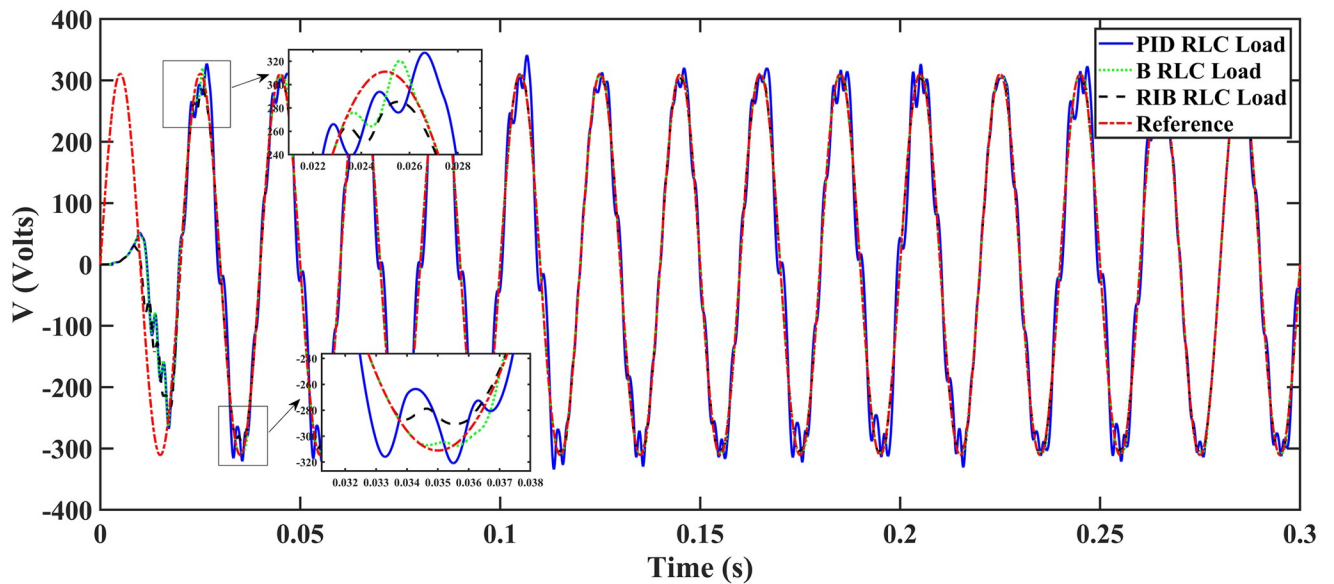


Fig 21. Inverter output voltage at resistive, inductive, and capacitive loads after filtering.

<https://doi.org/10.1371/journal.pone.0297612.g021>

controller, respectively, at a 50Hz frequency, while the THD is 20.13%, 14.22%, and 13.04%. This means that the RMS magnitude of harmonic frequencies are 20.13%, 14.22%, and 13.04% of the RMS magnitude of the fundamental frequency. The RIB controller shows better harmonic distortion compared to benchmark controllers, which is less than 5% according to the IEEE standard. As is evident from Fig 22, the THD due to proposed controller converges to zero level earlier than the PID and back-stepping controllers. In other words, the proposed controller as fewer harmonics in the output of the inverter. The performance indices of the inverter output voltage is calculated in Fig 23 and are compared in Table 6. Fig 23 shows the tracking error in terms of four error metrics. As can be seen from the figures, PID controller has the largest error and the proposed controller has the minimum error. In addition, Fig 17 (b) and 17(d) shows that the tracking error due to PID controller keeps on increasing and does not converge in finite time. The inverter, evaluated with the suggested controller in standalone mode, has low harmonic distortion, strong control performance, and a high-quality sinusoidal waveform, as can be concluded from Figs 21–23.

4.2 Transient performance of the inverter output voltage with the different load when the reference amplitude changes in step

4.2.1 Scenario 4 When the reference amplitude changes in step. The MPPT results are the same as discussed in the previous section, they remain consistent for all loads. In scenario 4, a resistive load, when the reference amplitude changed in steps. The inverter's output voltage with a resistive load under step changes in reference amplitude are displayed in Fig 24. Step changes mean that from 0.1s to 0.2s, the amplitude of the reference voltage changed from 311V to 371V and then back to 311V to check the transient performance of the system. The results show that the output voltage perfectly tracks the new reference voltage with good approximation and stability, by the proposed technique. The proposed controller tracks the reference voltage in almost 0.01s, while the back-stepping and PID controllers track it in 0.025s and 0.04s, respectively. As can be seen from Fig 24, the initial response of PID and

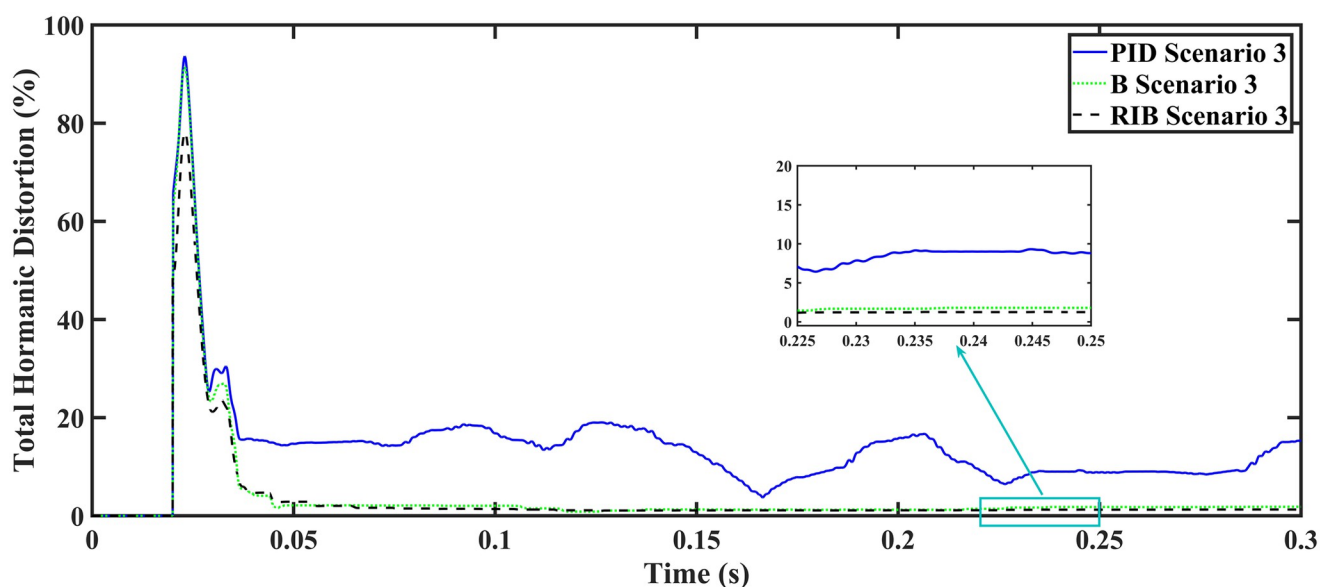


Fig 22. Total harmonic distortion.

<https://doi.org/10.1371/journal.pone.0297612.g022>

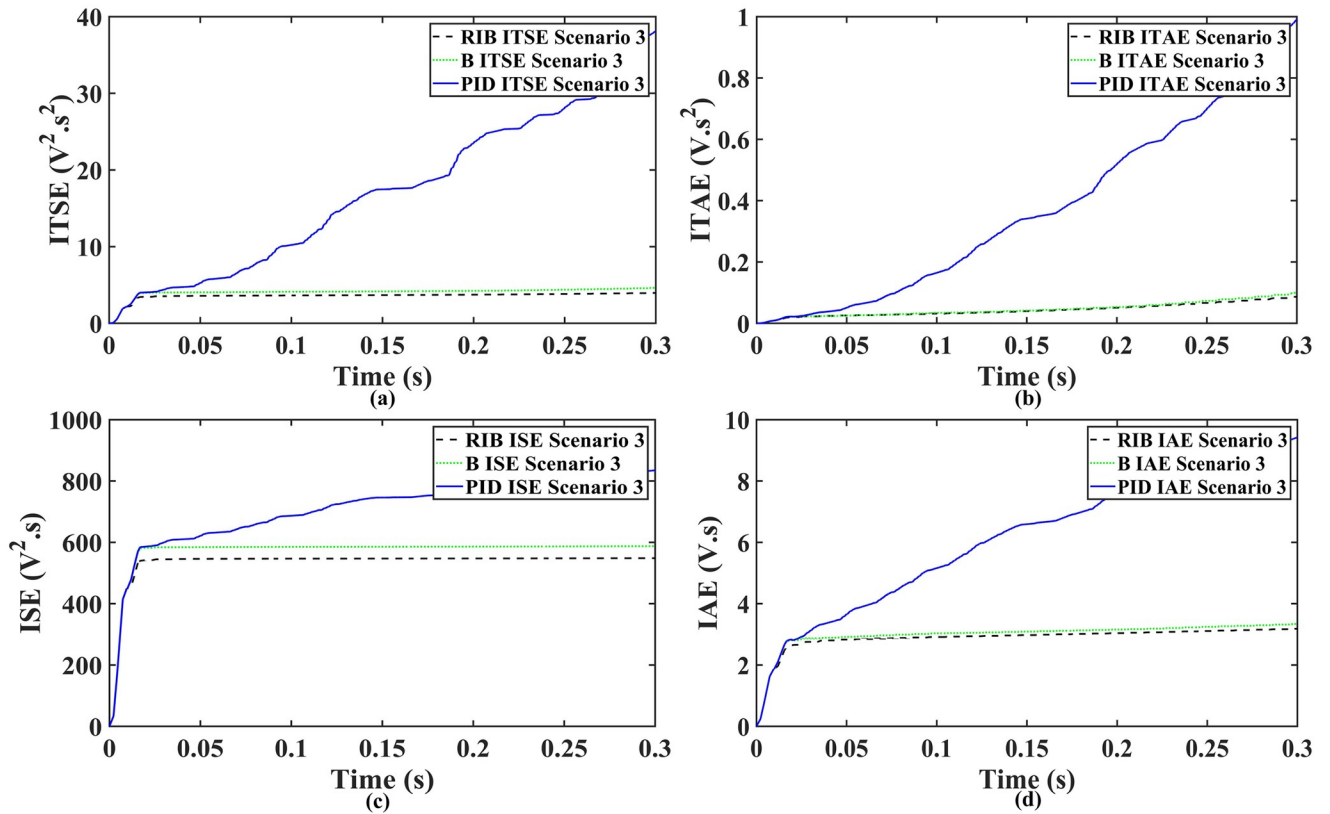


Fig 23. Performance indices of inverter output voltage with resistive, inductive, and capacitive loads (a)ITSE (b)ITAE (c)ISE (d)IAE.

<https://doi.org/10.1371/journal.pone.0297612.g023>

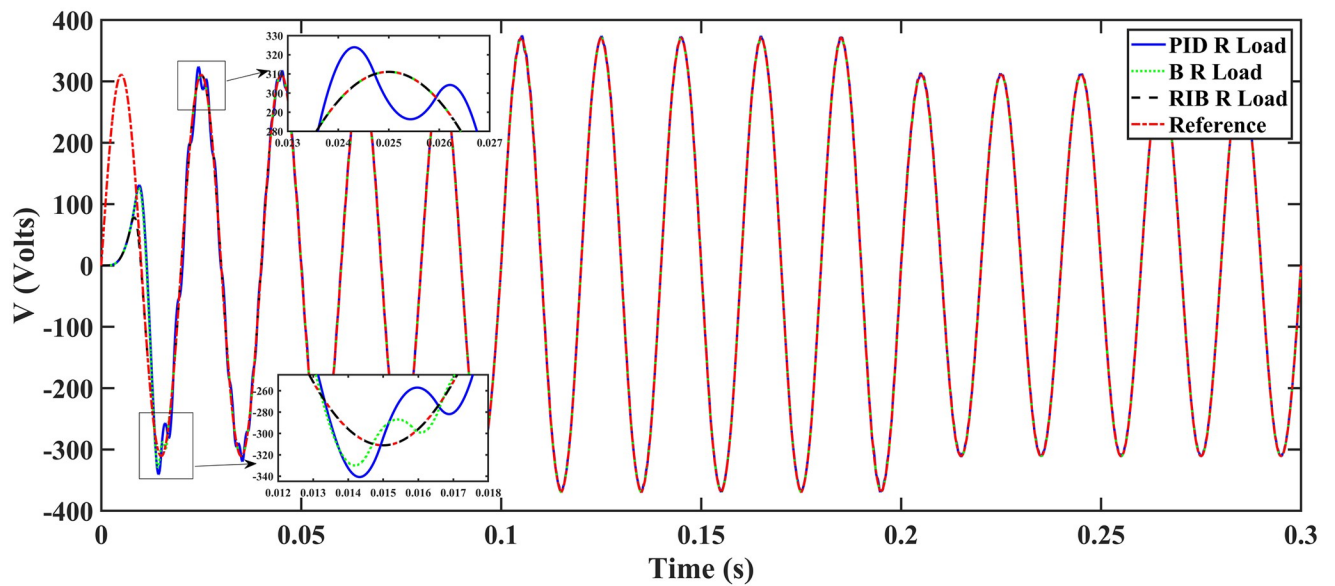


Fig 24. Inverter output voltage at resistive load after filtering under step changes in reference amplitude.

<https://doi.org/10.1371/journal.pone.0297612.g024>

back-stepping controllers have overshoots and undershoots, whereas the proposed controller has readily tracked the reference voltage from the start without any overshoot and undershoot. This also implies the convergence time of the proposed controller is smaller. If the inverter input voltage is less than 700V which is the nominal voltage of the inverter input, a drop appears in the output voltage. The distortion in the output voltage of the inverter at the beginning is due to the insufficient voltage provided by the non-inverting buck-boost converter. After 0.01s, in the case of the proposed controller, the input voltage of the inverter exceeds 700V and the output voltage of the inverter begins to track the reference voltage. The output voltage frequency analysis and RMSE are compared in Tables 4 and 5, respectively. The fundamental voltage is approximately 319.8V, 320.3V, and 320.8V in the case of the PID controller, back-stepping controller, and proposed controller, respectively, at a 50Hz frequency, while the THD is 14.27%, 13.82%, and 11.45%. This means that the RMS magnitude of harmonics frequencies are 14.27%, 13.82%, and 11.45% of the RMS magnitude of the fundamental frequency. The RIB controller exhibits better harmonic distortion compared to benchmark controllers, which is less than 5% according to the IEEE standard. As is evident from Fig 25, the THD due to proposed controller converges to zero level earlier than the PID and back-stepping controllers. In other words, the proposed controller has fewer harmonics in the output of the inverter. The performance indices of the inverter output voltage is calculated in Fig 26 and are compared in Table 7. Fig 26 shows the tracking error in terms of four error metrics. As can be seen from the figures, PID controller has the largest error and the proposed controller has the minimum error. In addition, Fig 17(b) and 17(d) shows that the tracking error due to PID controller keeps on increasing and does not converge in finite time. The inverter, evaluated with the suggested controller in standalone mode, demonstrates low harmonic distortion, strong control performance, and a high-quality sinusoidal waveform, as can be concluded from Figs 24–26.

4.2.2 Scenario 5 When the reference amplitude changes in step. We assume a resistive inductive loads in scenario 5, where the reference amplitude changes in steps. The inverter's output voltage with a resistive inductive loads when the reference amplitude changes in steps

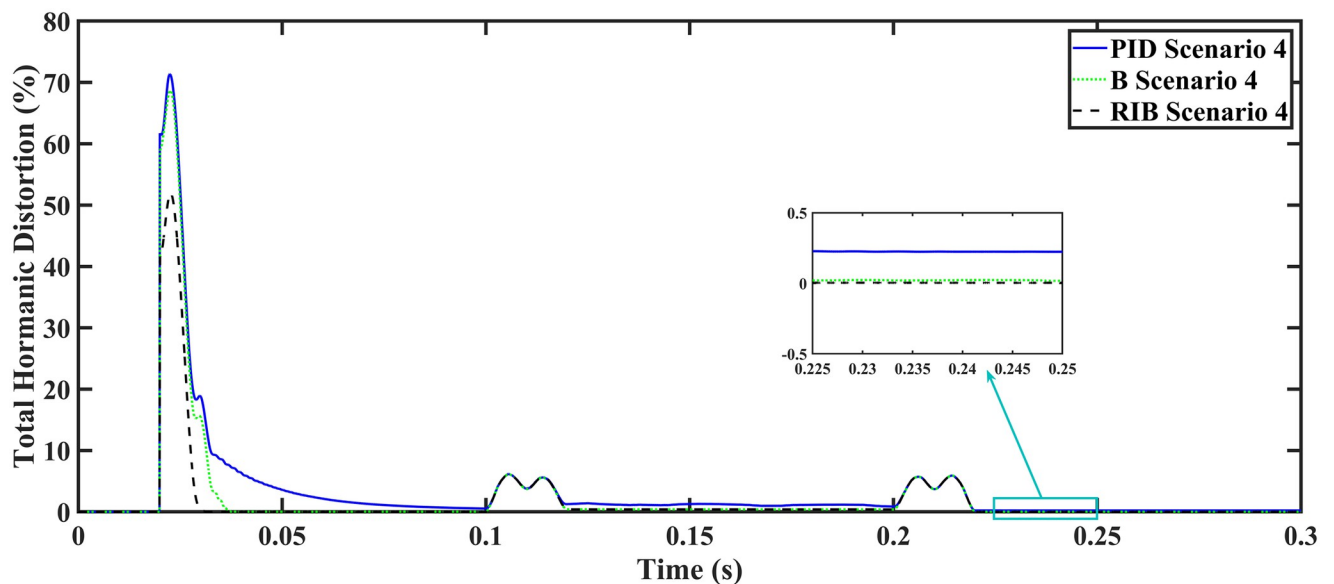


Fig 25. Total harmonic distortion.

<https://doi.org/10.1371/journal.pone.0297612.g025>

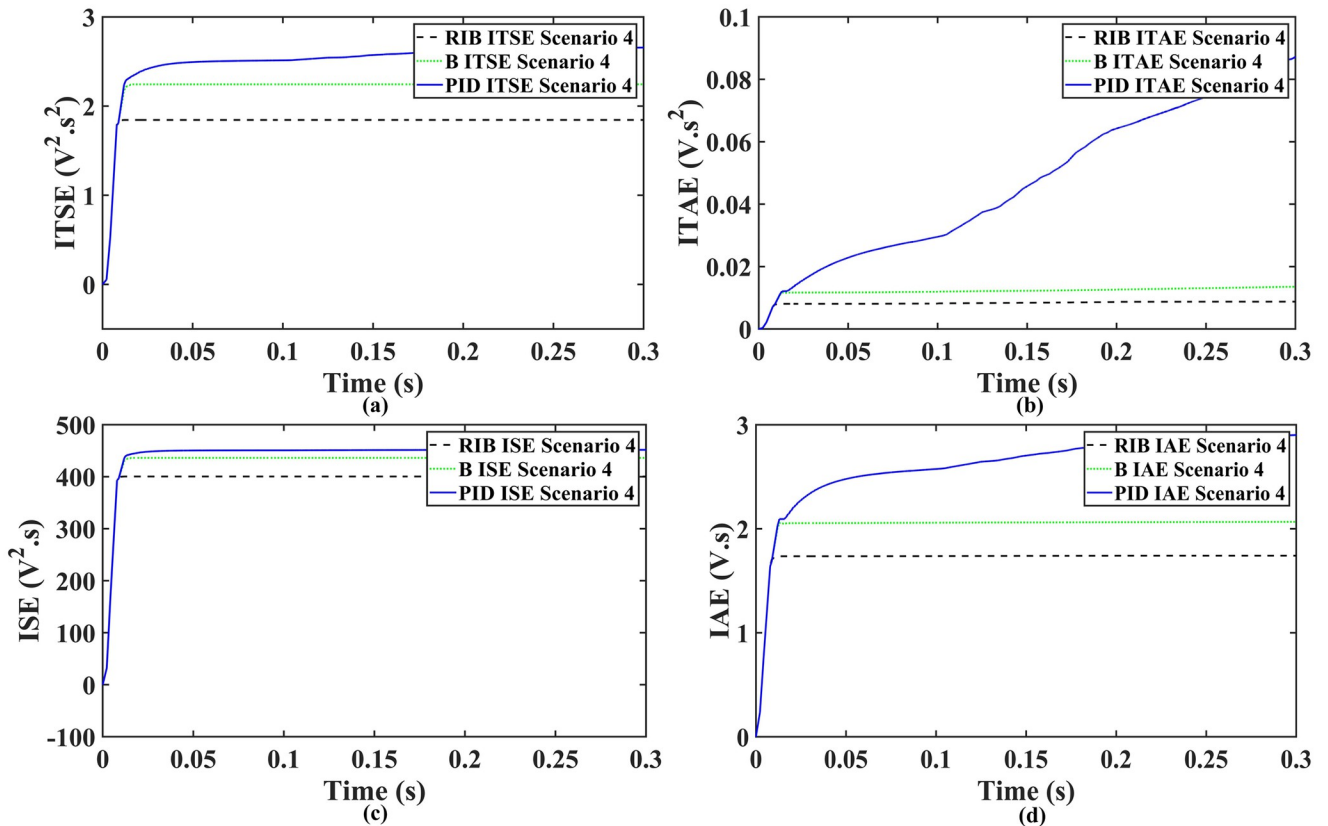


Fig 26. Performance indices of inverter output voltage with resistive load when the reference amplitude changes in step (a)ITSE (b)ITAE (c)ISE (d) IAE.

<https://doi.org/10.1371/journal.pone.0297612.g026>

are shown in Fig 27. Step changes mean that from 0.1s to 0.2s, the amplitude of the reference voltage changes from 311V to 371V and then back to 311V to assess the transient performance of the system. The results show that the output voltage perfectly tracks the new reference voltage with good approximation and stability, due to the proposed technique. The proposed controller tracks the reference voltage in almost 0.01s, while the back-stepping and PID controllers track it in 0.025s and 0.04s. As can be seen from Fig 27, the initial response of PID and back-stepping controllers have overshoots and undershoots, whereas the proposed controller has readily tracked the reference voltage from the start without any overshoot and undershoot. This also implies the convergence time of the proposed controller is smaller. If the inverter input voltage is less than 700V which is the nominal voltage of the inverter input, a drop appears in the output voltage. The distortion in the output voltage of the inverter at the beginning is due to insufficient voltage provided by the non-inverting buck-boost converter. After 0.01s, in the case of the proposed controller, the input voltage of the inverter exceeds 700V and the output voltage of the inverter begins to track the reference voltage. The output voltage frequency analysis and RMSE are compared in Tables 4 and 5, respectively. The fundamental voltage is approximately 319.7V, 320.3V, and 320.8V in the case of the PID controller, back-stepping controller, and proposed controller, respectively, at a 50Hz frequency, while the THD is 14.28%, 13.82%, and 11.45%. This means that the RMS magnitude of harmonic frequencies are 14.28%, 13.82%, and 11.45% of the RMS magnitude of the fundamental frequency. The RIB controller exhibits better harmonic distortion compared to benchmark controllers, which

Table 7. Comparison of ITSE, ITAE, ISE and IAE under step changes in reference amplitude.

Scenario	Scenario 1			Scenario 2			Scenario 3		
	PID	B	RIB	PID	B	RIB	PID	B	RIB
ITSE	2.656	2.244	1.844	2.807	2.251	1.855	47.59	7.064	6.044
ITAE	0.0872	0.0135	0.0087	0.0189	0.0142	0.0088	1.152	0.1997	0.1522
ISE	451.6	436.1	400.3	452.8	436.7	401	889.8	603.8	563.1
IAE	2.902	2.066	1.741	3.07	2.123	1.763	10.24	3.989	3.637

<https://doi.org/10.1371/journal.pone.0297612.t007>

is less than 5% according to the IEEE standard. As is evident from Fig 28, the THD due to proposed controller converges to zero level earlier than the PID and back-stepping controllers. In other words, the proposed controller has fewer harmonics in the output of the inverter. The performance indices of the inverter output voltage is calculated in Fig 29 and are compared in Table 7. Fig 29 shows the tracking error in terms of four error metrics. As can be seen from the figures, PID controller has the largest error and the proposed controller has the minimum error. In addition, Fig 17(b) and 17(d) shows that the tracking error due to PID controller keeps on increasing and does not converge in finite time. The inverter, evaluated with the suggested controller in standalone mode, has low harmonic distortion, strong control performance, and a high-quality sinusoidal waveform, as can be concluded from Figs 27–29.

4.2.3 Scenario 6 When the reference amplitude changes in step. A resistive, inductive, and capacitive loads is employed in scenario 6, where the reference amplitude changes in steps. The inverter’s output voltage with a resistive, inductive, and capacitive loads when the reference amplitude changes in steps is shown in Fig 30. Step changes mean that from 0.1s to 0.2s, the amplitude of the reference voltage changes from 311V to 371V and then back to 311V to assess the transient performance of the system. The results show that the output voltage perfectly tracks the new reference voltage with good approximation and stability, by the proposed technique. As can be seen from Fig 30, the initial response of PID and back-stepping controllers have overshoots and undershoots, whereas the proposed controller has readily tracked the

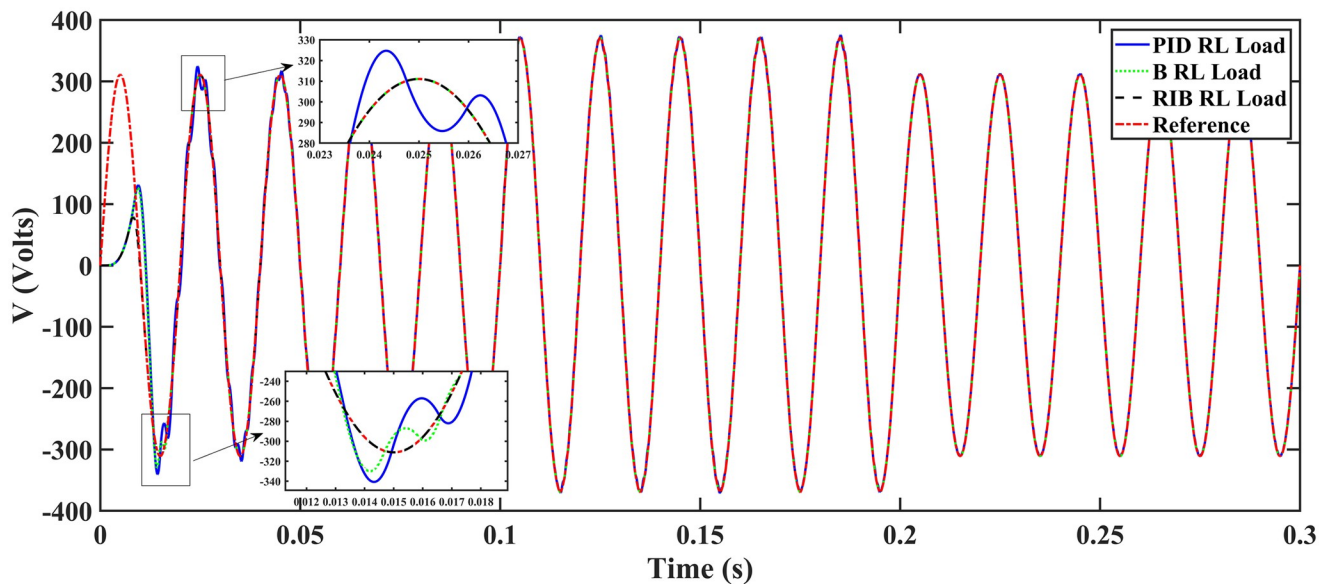


Fig 27. Inverter output voltage at resistive inductive loads after filtering under step changes in reference amplitude.

<https://doi.org/10.1371/journal.pone.0297612.g027>

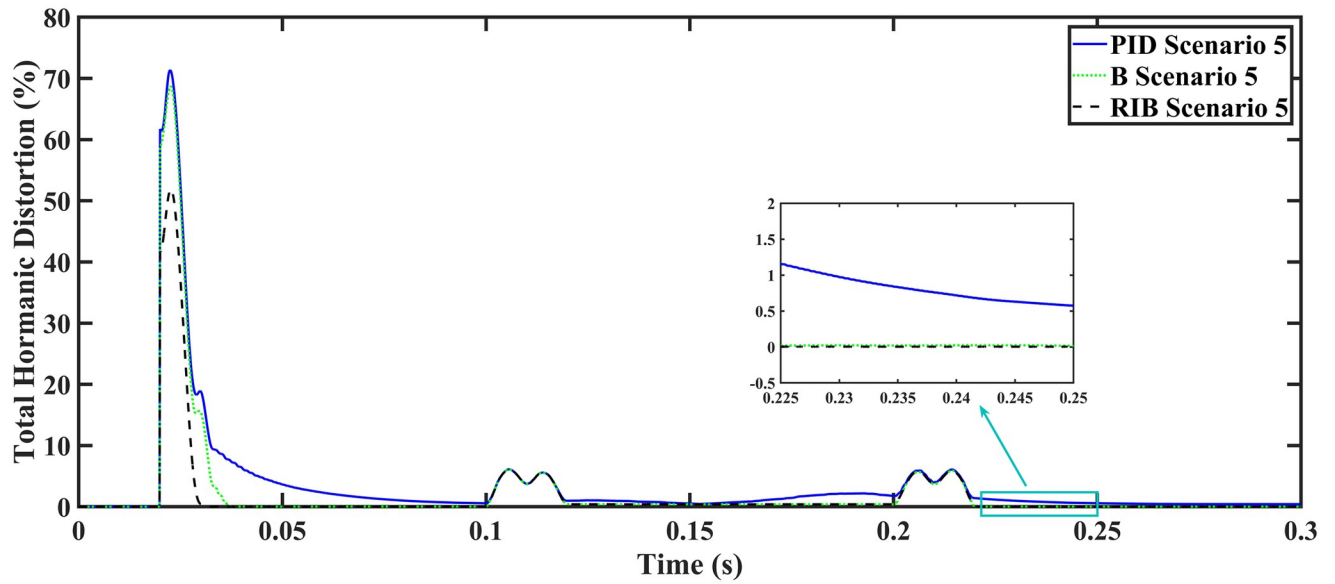


Fig 28. Total harmonic distortion.

<https://doi.org/10.1371/journal.pone.0297612.g028>

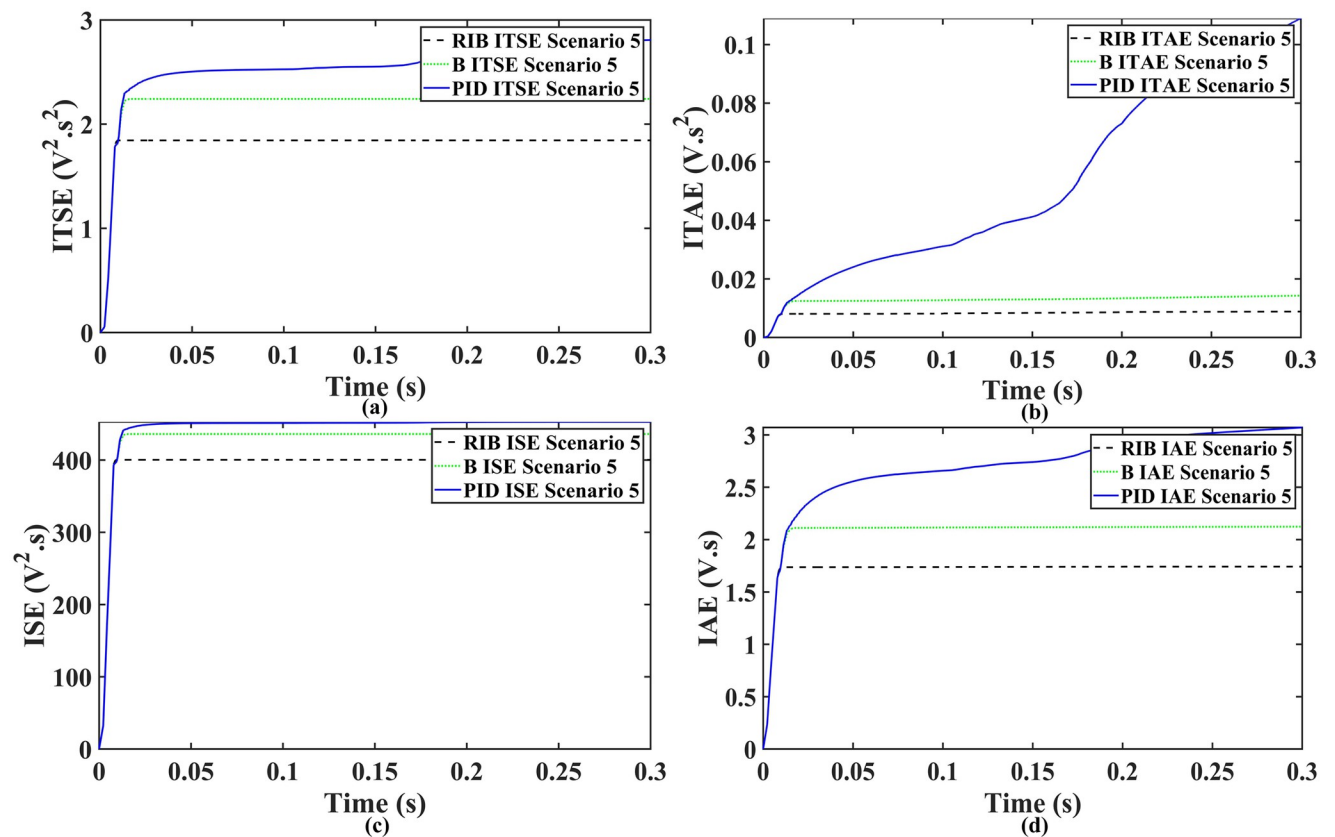


Fig 29. Performance indices of inverter output voltage with the resistive inductive loads when the reference amplitude changes in step (a)ITSE (b) ITAE (c)ISE (d)IAE.

<https://doi.org/10.1371/journal.pone.0297612.g029>

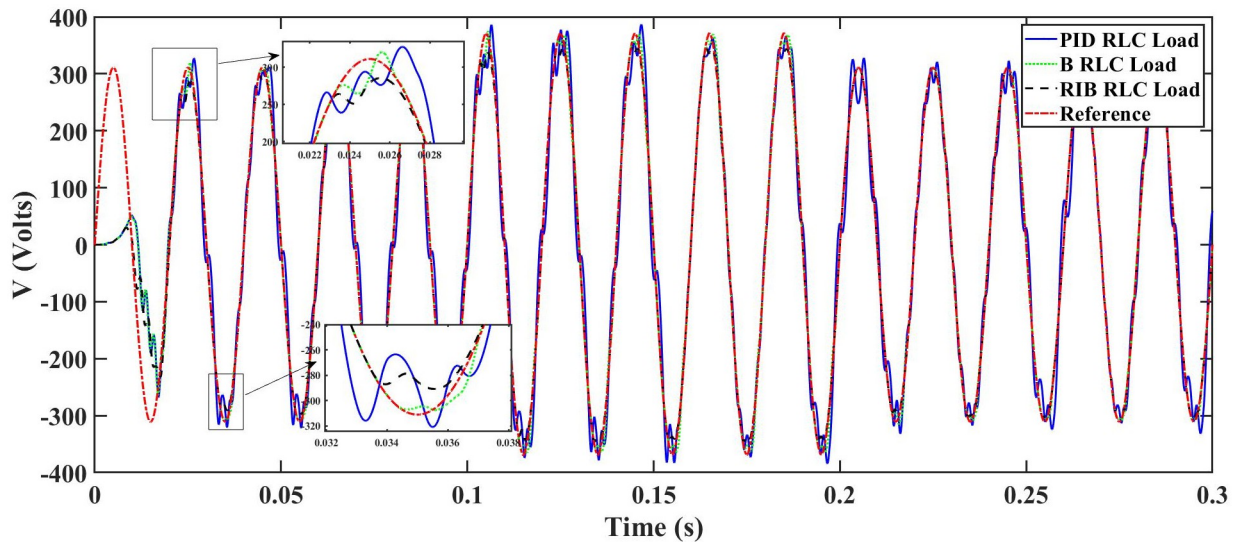


Fig 30. Inverter output voltage at resistive, inductive, and capacitive loads after filtering under step changes in reference amplitude.

<https://doi.org/10.1371/journal.pone.0297612.g030>

reference voltage from the start without any overshoot and undershoot. This also implies the convergence time of the proposed controller is smaller. This means that the proposed controller tracks the reference voltage faster compared to the benchmark controller. If the inverter input voltage is less than 700V which is the nominal voltage of the inverter input, a drop appears in the output voltage. The distortion in the output voltage of the inverter at the beginning is due to insufficient voltage provided by the non-inverting buck-boost converter. After 0.01s, in the case of the proposed controller, the input voltage of the inverter exceeds 700V and the output voltage of the inverter begins to track the reference voltage. The output voltage frequency analysis and RMSE are compared in Tables 4 and 5, respectively. The fundamental voltage is approximately 314.1V, 316.4V, and 310.3V in the case of the PID controller, back-stepping controller, and proposed controller, respectively, at a 50Hz frequency, while the THD is 21.57%, 15.76%, and 14.33%. This means that the RMS magnitude of harmonic frequencies are 21.57%, 15.76%, and 14.33% of the RMS magnitude of the fundamental frequency. The RIB controller exhibits better harmonic distortion compared to benchmark controllers, which is less than 5% according to the IEEE standard. As is evident from Fig 16, the THD due to proposed controller converges to zero level earlier than the PID and back-stepping controllers. In other words, the proposed controller has fewer harmonics in the output of the inverter. The performance indices of the inverter output voltage is calculated in Fig 32 and are compared in Table 7. Fig 32 shows the tracking error in terms of four error metrics. As can be seen from the figures, PID controller has the largest error and the proposed controller has the minimum error. In addition, Fig 17(b) and 17(d) shows that the tracking error due to PID controller keeps on increasing and does not converge in finite time. The inverter, evaluated with the suggested controller in standalone mode, demonstrates low harmonic distortion, strong control performance, and a high-quality sinusoidal waveform, as can be concluded from Figs 30–32.

5. Conclusion

In this paper, a robust integral back-stepping nonlinear MPPT algorithm for single-phase PV inverters is designed to extract the maximum power under varying environmental conditions. The proposed techniques are analyzed in two different scenarios: 1) Steady-state performance

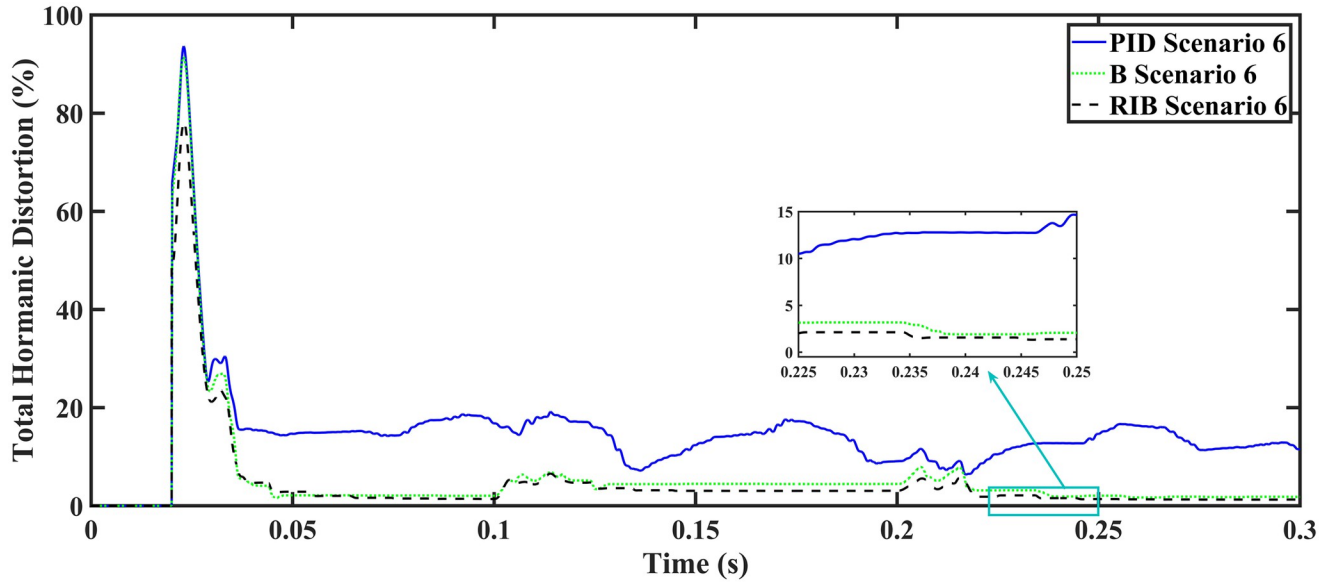


Fig 31. Total harmonic distortion.

<https://doi.org/10.1371/journal.pone.0297612.g031>

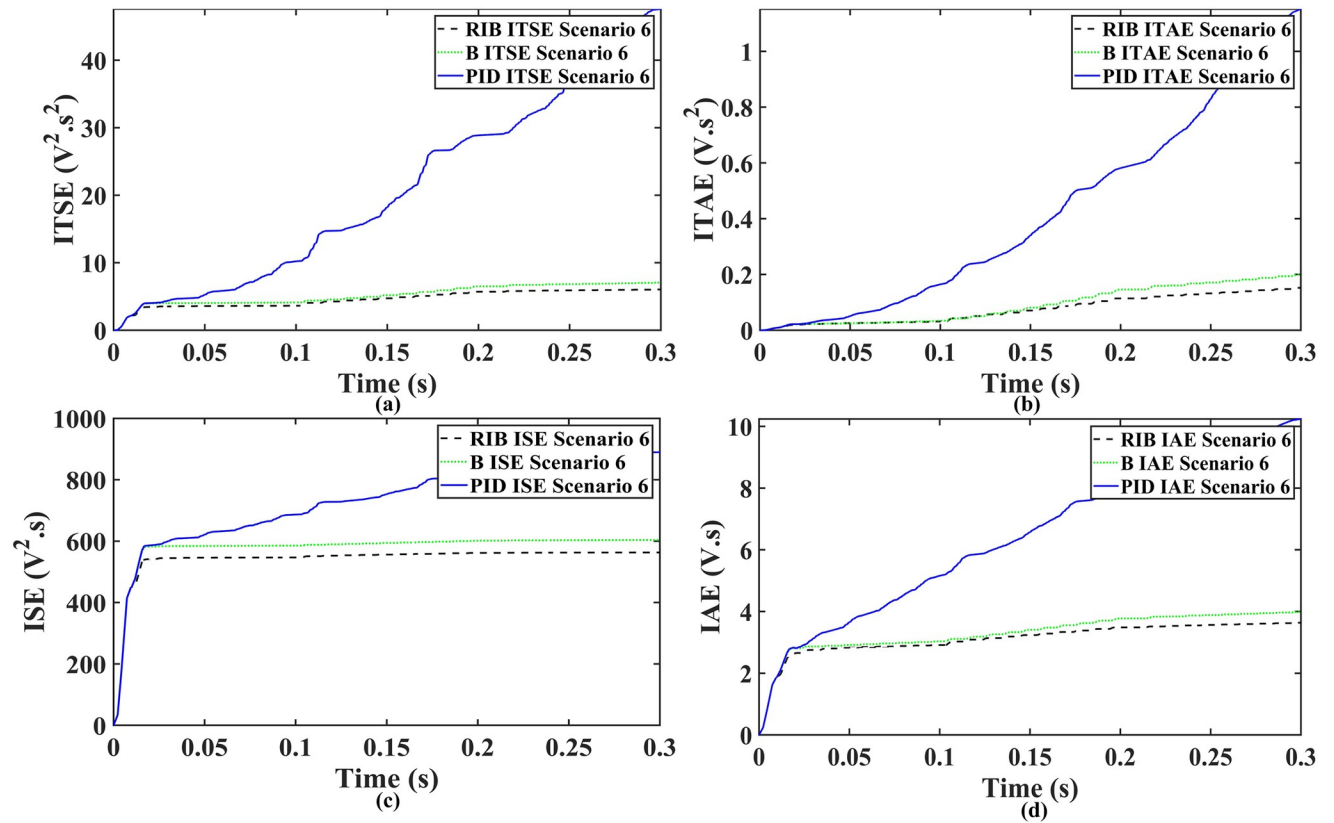


Fig 32. Performance indices of inverter output voltage with resistive inductive and capacitive loads when the reference amplitude changes in step (a) ITSE (b)ITAE (c)ISE (d)IAE.

<https://doi.org/10.1371/journal.pone.0297612.g032>

of the output voltage of the inverter with different loads 2) Transient performance of the output voltage of inverter with different loads under step changes in reference amplitude. A reference voltage is generated through a regression plane based on the changes in environmental conditions. The simulation results demonstrate two key achievements. First, the extraction of a maximum power from the PV module using a nonlinear robust integral back-stepping controller in conjunction with a buck-boost converter. Second, the generation of sinusoidal waveform for the inverter's output voltage, either at 311V (peak-peak) or 220V (RMS) with a fixed frequency of 50Hz. These results are assessed using the RIBSC, which effectively minimizes the convergence error. Simulation results also indicate that the proposed controller has a lower THD in comparison to both the back-stepping controller and the conventional PID controller.

Author Contributions

Conceptualization: Laiq Khan.

Data curation: Adil Latif, Sidra Mumtaz.

Formal analysis: Adil Latif, Laiq Khan.

Investigation: Laiq Khan, Sidra Mumtaz, Jamshed Iqbal.

Methodology: Adil Latif, Shahrukh Agha.

Project administration: Jamshed Iqbal.

Resources: Jamshed Iqbal.

Software: Adil Latif, Shahrukh Agha, Sidra Mumtaz.

Supervision: Laiq Khan.

Validation: Jamshed Iqbal.

Visualization: Shahrukh Agha, Sidra Mumtaz.

Writing – original draft: Adil Latif, Laiq Khan, Shahrukh Agha.

Writing – review & editing: Jamshed Iqbal.

References

1. Ellabban O, Abu-Rub H, Blaabjerg F. Renewable energy resources: Current status, future prospects and their enabling technology. *Renewable and Sustainable Energy Reviews*. 2014 Nov 1; 39:748–64. <https://doi.org/10.1016/j.rser.2014.07.113>
2. Saleem O, Ali S, Iqbal J. Robust MPPT Control of Stand-Alone Photovoltaic Systems via Adaptive Self-Adjusting Fractional Order PID Controller. *Energies*. 2023 Jun 29; 16(13):5039. <https://doi.org/10.3390/en16135039>
3. Morales-Caporal M, Rangel-Magdaleno J, Peregrina-Barreto H, Morales-Caporal R. FPGA-in-the-loop simulation of a grid-connected photovoltaic system by using a predictive control. *Electrical Engineering*. 2018 Sep 1; 100(3):1327–37. <https://doi.org/10.1007/s00202-017-0596-1>
4. Yang Y, Blaabjerg F. Overview of single-phase grid-connected photovoltaic systems. *Electric Power Components and Systems*. 2015 Jul 21; 43(12):1352–63. <https://doi.org/10.1080/15325008.2015.1031296>
5. Irfan M, Iqbal J, Iqbal A, Iqbal Z, Riaz RA, Mehmood A. Opportunities and challenges in control of smart grids—Pakistani perspective. *Renewable and Sustainable Energy Reviews*. 2017; 71:652–674. <https://doi.org/10.1016/j.rser.2016.12.095>
6. Hassaine L. Power converters and control of grid-connected photovoltaic systems. In *Renewable Energy in the Service of Mankind Vol II 2016* (pp. 497–504). Springer, Cham.
7. Ali Khan MY, Liu H, Yang Z, Yuan X. A comprehensive review on grid connected photovoltaic inverters, their modulation techniques, and control strategies. *Energies*. 2020 Aug 13; 13(16):4185. <https://doi.org/10.3390/en13164185>

8. Ayop R, Tan CW. Design of boost converter based on maximum power point resistance for photovoltaic applications. *Solar Energy*. 2018 Jan 15; 160:322–35. <https://doi.org/10.1016/j.solener.2017.12.016>
9. Martin AD, Vazquez JR. MPPT algorithms comparison in PV systems: P&O, PI, neuro-fuzzy and backstepping controls. In 2015 IEEE International Conference on Industrial Technology (ICIT) 2015 Mar 17 (pp. 2841–2847). IEEE.
10. Hassan A, Bass O, Masoum MA. An improved genetic algorithm based fractional open circuit voltage MPPT for solar PV systems. *Energy Reports*. 2023 Dec 1; 9:1535–48. <https://doi.org/10.1016/j.egy.2022.12.088>
11. Motahhir S, El Hammoumi A, El Ghzizal A. Photovoltaic system with quantitative comparative between an improved MPPT and existing INC and P&O methods under fast varying of solar irradiation. *Energy Reports*. 2018 Nov 1; 4:341–50. <https://doi.org/10.1016/j.egy.2018.04.003>
12. Cheddadi Y, Errahimi F, Es-sbai N. Design and verification of photovoltaic MPPT algorithm as an automotive-based embedded software. *Solar Energy*. 2018 Sep 1; 171:414–25. <https://doi.org/10.1016/j.solener.2018.06.085>
13. Arsalan M, Iftikhar R, Ahmad I, Hasan A, Sabahat K, Javeria A., et al. MPPT for photovoltaic system using nonlinear backstepping controller with integral action. *Solar Energy*. 2018 Aug 1; 170:192–200. <https://doi.org/10.1016/j.solener.2018.04.061>
14. Kaouane M, Boukhelifa A, Cheriti A. Regulated output voltage double switch Buck-Boost converter for photovoltaic energy application. *International Journal of Hydrogen Energy*. 2016 Dec 7; 41(45):20847–57. <https://doi.org/10.1016/j.ijhydene.2016.06.140>
15. Chen Zhi, Melvyn S, and Peng X. Robust Stochastic Optimization to design a controller to get maximum power. *History* (2019).
16. Keshavarz M, Doroudi A, Kazemi MH, Dehkordi NM. A Novel Hybrid Droop-Isochronous Control Strategy for Microgrid Management. *Iranian Journal of Electrical & Electronic Engineering*. 2021 Jun 1; 17(2).
17. Alqatamin M, McIntyre ML. Nonlinear backstepping controller for single-phase grid-connected inverters. In 2019 20th Workshop on Control and Modeling for Power Electronics (COMPEL) 2019 Jun 17 (pp. 1–6). IEEE.
18. Diouri O, Errahimi F, Es-Sbai N. Regulation of the output voltage of an inverter in case of load variation. *INOP Conference Series: Materials Science and Engineering* 2018 May (Vol. 353).
19. Wang Z, Li S, Li Q. Discrete-time fast terminal sliding mode control design for DC–DC buck converters with mismatched disturbances. *IEEE Transactions on Industrial Informatics*. 2019 Aug 27; 16(2):1204–13. <https://doi.org/10.1109/TII.2019.2937878>
20. Lee DC, Lee GM. Linear control of inverter output voltage in overmodulation. *IEEE Transactions on Industrial Electronics*. 1997 Aug; 44(4):590–2. <https://doi.org/10.1109/41.605640>
21. Kim IS, Youn MJ. Variable-structure observer for solar-array current estimation in a photovoltaic power-generation system. *IEE Proceedings-Electric Power Applications*. 2005 Jul 1; 152(4):953–9. <https://doi.org/10.1049/ip-epa:20045245>
22. Hasanzadeh A, Edrington CS, Maghsoudlou B, Fleming F, Mokhtari H. Multi-loop linear resonant voltage source inverter controller design for distorted loads using the linear quadratic regulator method. *IET Power Electronics*. 2012 Jul 1; 5(6):841–51. <https://doi.org/10.1049/iet-pel.2011.0400>
23. Koiwa K, Goto T, Zanma T, Liu KZ. Passivity-Based Robust Controller Design for Load-Independent Voltage Source Inverters. *IEEE Access*. 2022 Dec 20; 10:132742–51. <https://doi.org/10.1109/ACCESS.2022.3230967>
24. Zadeh AK, Kashkooli LI, Mirzaee SA. Designing a power inverter and comparing back-stepping, sliding-mode and fuzzy controllers for a single-phase inverter in an emergency power supply. *Ciência e Natura*. 2015 Dec 19; 37:175–81.
25. Kolbasi E, Seker M. Nonlinear robust backstepping control method approach for single phase inverter. In 2016 21st International Conference on Methods and Models in Automation and Robotics (MMAR) 2016 (pp. 954–958). IEEE.
26. Zhang X, He J, Ma H, Ma Z, Ge X. An Adaptive Dual-Loop Lyapunov-Based Control Scheme for a Single-Phase Stand-Alone Inverter to Improve Its Large-Signal Stability. In *Stability Enhancement Methods of Inverters Based on Lyapunov Function, Predictive Control, and Reinforcement Learning* 2022 Nov 30 (pp. 33–46). Singapore: Springer Nature Singapore.
27. Afifa R, Ali S, Pervaiz M, Iqbal J. Adaptive backstepping integral sliding mode control of a MIMO separately excited DC Motor. *Robotics*. 2023; 12(4),105. <https://doi.org/10.3390/robotics12040105>
28. Hosseini SK, Mehrasa M, Taheri S, Rezanejad M, Pouresmaeil E, Catalão JP., et al. A control technique for operation of single-phase converters in stand-alone operating mode. In 2016 IEEE Electrical Power and Energy Conference (EPEC) 2016 Oct 12 (pp. 1–6). IEEE.

29. Xue Y, Chang L, Kjaer SB, Bordonau J, Shimizu T. Topologies of single-phase inverters for small distributed power generators: an overview. *IEEE transactions on Power Electronics*. 2004 Sep 3; 19(5):1305–14. <https://doi.org/10.1109/TPEL.2004.833460>
30. Abadi M, Sadeghzadeh SM. A control approach with seamless transition capability for a single-phase inverter operating in a microgrid. *International Journal of Electrical Power & Energy Systems*. 2019 Oct 1; 111:475–85. <https://doi.org/10.1016/j.ijepes.2019.04.012>
31. Anjum MB, Khan Q, Ullah S, Hafeez G, Fida A, Iqbal J, et al. Maximum power extraction from a stand-alone photo voltaic system via neuro-adaptive arbitrary order sliding mode control strategy with high gain differentiation. *Applied Sciences*. 2022 Mar 8; 12(6):2773. <https://doi.org/10.3390/app12062773>
32. Ahmad S, Uppal AA, Azam MR, Iqbal J. Chattering free sliding mode control and state dependent Kalman filter design for underground coal gasification energy conversion process. *Electronics*. 2023; 12(4):876 <https://doi.org/10.3390/electronics12040876>
33. Armghan H, Ahmad I, Armghan A, Khan S, Arsalan M. Backstepping based non-linear control for maximum power point tracking in photovoltaic system. *Solar Energy*. 2018 Jan 1; 159:134–41. <https://doi.org/10.1016/j.solener.2017.10.062>
34. Arsalan M, Iftikhar R, Ahmad I, Hasan A, Sabahat K, Javeria A., et al. MPPT for photovoltaic system using nonlinear backstepping controller with integral action. *Solar Energy*. 2018 Aug 1; 170:192–200. <https://doi.org/10.1016/j.solener.2018.04.061>
35. Diouri O, Es-Sbai N, Errahimi F, Gaga A, Alaoui C. Modeling and Design of Single-Phase PV Inverter with MPPT Algorithm Applied to the Boost Converter Using Back-Stepping Control in Standalone Mode. *International Journal of Photoenergy*. 2019 Nov 6; 2019. <https://doi.org/10.1155/2019/7021578>
36. Ali K, Khan Q, Ullah S, Khan I, Khan L. Nonlinear robust integral backstepping based MPPT control for stand-alone photovoltaic system. *Plos one*. 2020 May 19; 15(5):e0231749. <https://doi.org/10.1371/journal.pone.0231749> PMID: 32427990
37. Khan ZA, Khan L, Ahmad S, Mumtaz S, Jafar M, Khan Q., et al. RBF neural network based backstepping terminal sliding mode MPPT control technique for PV system. *Plos one*. 2021 Apr 8; 16(4):e0249705. <https://doi.org/10.1371/journal.pone.0249705> PMID: 33831094
38. Priyadarshi N, Padmanaban S, Holm-Nielsen JB, Blaabjerg F, Bhaskar MS. An experimental estimation of hybrid ANFIS–PSO-based MPPT for PV grid integration under fluctuating sun irradiance. *IEEE Systems Journal*. 2019 Nov 15; 14(1):1218–29. <https://doi.org/10.1109/JSYST.2019.2949083>
39. Priyadarshi N, Padmanaban S, Maroti PK, Sharma A. An extensive practical investigation of FPSO-based MPPT for grid integrated PV system under variable operating conditions with anti-islanding protection. *IEEE Systems Journal*. 2018 Apr 9; 13(2):1861–71. <https://doi.org/10.1109/JSYST.2018.2817584>
40. Priyadarshi N, Sanjeevikumar P, Bhaskar MS, Azam F, Taha IB, Hussien MG. An adaptive TS-fuzzy model based RBF neural network learning for grid integrated photovoltaic applications. *IET Renew Power Gener* 16 (14): 3149–3160. <https://doi.org/10.1049/rpg2.12505>
41. Salem A, Abido MA. T-type multilevel converter topologies: A comprehensive review. *Arabian Journal for Science and Engineering*. 2019 Mar 11; 44(3):1713–35. <https://doi.org/10.1007/s13369-018-3506-6>
42. Chandel TA, Yasin MY, Mallick MA. Modeling and simulation of photovoltaic cell using single diode solar cell and double diode solar cell model. *Int. J. Innovative Technol. Explor. Eng.(IJITEE)*. 2019 Aug; 8(10).
43. Prakash SB, Singh G, Singh S. Modeling and performance analysis of simplified two-diode model of photovoltaic cells. *Frontiers in Physics*. 2021 Oct 25; 9:690588. <https://doi.org/10.3389/fphy.2021.690588>
44. Dehghani M, Taghipour M, Gharehpetian GB, Abedi M. Optimized fuzzy controller for MPPT of grid-connected PV systems in rapidly changing atmospheric conditions. *Journal of Modern Power Systems and Clean Energy*. 2020 May 19; 9(2):376–83. <https://doi.org/10.35833/MPCE.2019.000086>
45. Premkumar M, Kumar C, Sowmya R. Mathematical Modelling of Solar Photovoltaic Cell/Panel/Array based on the Physical Parameters from the Manufacturer's Datasheet. *International Journal of Renewable Energy Development*. 2020 Feb; 9(1):7–22. <https://doi.org/10.14710/ijred.9.1.7-22>
46. Kumar DD, Challa B, Ponnambalam P. A flyback partial power processing converter based solar PV systems interfacing the grid. In *2019 Innovations in Power and Advanced Computing Technologies (i-PACT) 2019 Mar 22 (Vol. 1, pp. 1–4)*. IEEE.
47. Khalil HK, Grizzle J. *Nonlinear systems*. vol. 3 Prentice hall. New Jersey. 1996.
48. Morey M, Gupta N, Garg MM, Kumar A. A comprehensive review of grid-connected solar photovoltaic system: Architecture, control, and ancillary services. *Renewable Energy Focus*. 2023 Jun 1; 45:307–30. <https://doi.org/10.1016/j.ref.2023.04.009>